

A radially broad collisional cascade in the debris disk of γ Ophiuchi observed by JWST

YINUO HAN ,¹ MARK WYATT ,² KATE Y. L. SU ,³ ANTRANIK A. SEFILIAN ,⁴ JOSHUA B. LOVELL ,⁵ CARLOS DEL BURGO ,^{6,7} JONATHAN P. MARSHALL ,⁸ SEBASTIAN MARINO ,⁹ DAVID J. WILNER ,⁵ BRENDA C. MATTHEWS ,^{10,11} MAX SOMMER ,² A. MEREDITH HUGHES ,¹² JOHN M. CARPENTER ,¹³ MEREDITH A. MACGREGOR ,¹⁴ NICOLE PAWELLEK ,¹⁵ AND THOMAS HENNING ,¹⁶

¹Division of Geological and Planetary Sciences, California Institute of Technology, 1200 E. California Blvd., Pasadena, CA 91125, USA

²Institute of Astronomy, University of Cambridge, Madingley Road, Cambridge, CB3 0HA, UK

³Space Science Institute, 4750 Walnut Street, Suite 205, Boulder, CO 80301, USA

⁴Department of Astronomy and Steward Observatory, University of Arizona, Tucson, AZ 85721, USA

⁵Center for Astrophysics, Harvard & Smithsonian, 60 Garden Street, Cambridge, MA 02138-1516, USA

⁶Instituto de Astrofísica de Canarias, Vía Láctea S/N, La Laguna, 38200, Tenerife, Spain

⁷Departamento de Astrofísica, Universidad de La Laguna, La Laguna, 38200, Tenerife, Spain

⁸Institute of Astronomy and Astrophysics, Academia Sinica, 11F of AS/NTU Astronomy-Mathematics Building, No. 1, Sec. 4, Roosevelt Rd, Taipei 106319, Taiwan

⁹Department of Physics and Astronomy, University of Exeter, Stocker Road, Exeter EX4 4QL, UK

¹⁰Herzberg Astronomy & Astrophysics Research Centre, National Research Council of Canada, 5071 West Saanich Road, Victoria, BC, Canada, V9E 2E7

¹¹Department of Physics & Astronomy, University of Victoria, 3800 Finnerty Rd, Victoria, BC, Canada, V8P 5C2

¹²Department of Astronomy, Van Vleck Observatory, Wesleyan University, 96 Foss Hill Dr., Middletown, CT, 06459, USA

¹³Joint ALMA Observatory, Avenida Alonso de Córdova 3107, Vitacura, Santiago, Chile

¹⁴Department of Physics and Astronomy, Johns Hopkins University, 3400 N Charles Street, Baltimore, MD 21218, USA

¹⁵Department of Astrophysics, University of Vienna, Türkenschanzstraße 17, 1180 Vienna, Austria

¹⁶Max Planck Institute for Astronomy, Königstuhl 17, 69117 Heidelberg, Germany

ABSTRACT

The A1V star γ Oph, at a distance of 29.7 pc, is known from Spitzer imaging to host a debris disk with a large radial extent and from its spectral energy distribution to host inner warm dust. We imaged γ Oph with JWST/MIRI at 15 and 25.5 μ m, which reveal smooth and radially broad emission that extends to a radius of at least 250 au at 25.5 μ m. In contrast to JWST findings of an inner small-grain component with distinct ringed substructures in Fomalhaut and Vega, the mid-infrared radial profile combined with prior ALMA imaging suggests a radially broad steady-state collisional cascade with the same grain size distribution throughout the disk. This further suggests that the system is populated by a radially broad planetesimal belt from tens of au or less to well over 200 au, rather than a narrow planetesimal belt from which the observed dust is displaced to appear broad. The disk is also found to be asymmetric, which could be modelled by a stellocentric offset corresponding to a small eccentricity of ~ 0.02 . Such a disk eccentricity could be induced by a mildly eccentric $< 10 M_{\text{Jup}}$ giant planet outside 10 au, or a more eccentric companion up to stellar mass at a few au, without producing a resolvable radial gap in the disk.

Keywords: Debris disks (363) — Circumstellar disks (235) — Planetary-disk interactions (2204) — Exoplanet systems (484) — Exoplanet evolution (491)

1. INTRODUCTION

Solid bodies in planetary systems initially assemble from dust embedded in gas-rich protoplanetary disks

(J. P. Williams & L. A. Cieza 2011). Following the dispersal of the primordial gas disk, planetesimals begin undergoing destructive mutual collisions, re-generating dust that populates a second-generation disk known as a debris disk (M. C. Wyatt 2008). These dust belts around main-sequence stars are some of the main ob-

servable signatures of extrasolar planetesimals (A. M. Hughes et al. 2018).

The structure of planetesimal belts are expected to inherit those of protoplanetary disks to some extent. Observationally, this is partly supported by similarities in the statistical distribution of ring widths in debris disks and protoplanetary disks (Y. Han et al. 2026). However, ongoing physical processes continue to shape debris disks. These dynamical processes generally occur in three categories. Firstly, solid bodies in debris disks frequently collide, producing successively smaller bodies down to micron-sized dust grains, forming a steady-state collisional cascade in which the size distribution can be characterised by a power law (J. S. Dohnanyi 1969; M. C. Wyatt et al. 2007; J. P. Marshall et al. 2025b). Dust grains smaller than a given threshold (in the micrometre regime) are ejected from the system by radiation pressure (J. A. Burns et al. 1979; A. V. Krivov 2010), thereby setting a minimum grain size. In addition to determining the grain size distribution, these collisions could influence the evolution of the disk structure, as collision rates are generally higher for closer-in orbits, resulting in faster depletion (G. M. Kennedy & M. C. Wyatt 2010). A collisionally eroded debris disk is expected to exhibit an inner edge surface density proportional to $r^{7/3}$ (G. M. Kennedy & M. C. Wyatt 2010; A. Imaz Blanco et al. 2023), and the outwards propagation of peak emission could contribute to the observed tentative increase in disk radius as a function of age on \sim 100 Myr timescales (C. Eiroa et al. 2013; L. Matrà et al. 2025; Y. Han et al. 2025).

Secondly, gravitational interactions with planets could perturb the distribution of the planetesimal belt within which dust is produced. For example, planets could carve sharper disk edges than that expected from collisional evolution alone (e.g., A. J. Mustill & M. C. Wyatt 2012; S. Marino 2021; A. Imaz Blanco et al. 2023; T. D. Pearce et al. 2024) or result in radial gaps (e.g. B. Yelverton & G. M. Kennedy 2018; M. F. Fribe et al. 2022; A. A. Sefilian et al. 2021, 2023), which have been observed in five debris disks based on Atacama Large Millimeter/sub-millimeter Array (ALMA) observations (S. Marino et al. 2018; M. A. MacGregor et al. 2019; C. Daley et al. 2019; S. Marino et al. 2019, 2020; A. Nederlander et al. 2021; Y. Han et al. 2026). Planets and/or stellar companions may also induce a non-zero disk eccentricity (M. C. Wyatt et al. 1999; T. D. Pearce & M. C. Wyatt 2014; M. A. Farhat et al. 2023), which can be further modulated by the disk's own gravity (A. A. Sefilian 2024). Planets that have migrated could further scatter planetesimals into high-eccentricity orbits, resulting in a scattered disk component, which has been suggested

to be the case in the Solar System's Kuiper Belt (R. Malhotra 1993; A. Morbidelli et al. 2004), HR8799 (F. Geiler et al. 2019), β Pic (L. Matrà et al. 2019) and η^1 Eri (J. B. Lovell et al. 2021).

Finally, stellar radiation displaces the spatial distribution of dust from their site of production (E. J. Lee & E. Chiang 2016). These effects include radiation pressure (L. E. Strubbe & E. I. Chiang 2006), which forces smaller grains produced from collisions onto higher eccentricity orbits until micron-sized grains are ejected from the system; and Poynting-Robertson drag (PR drag, M. C. Wyatt 2005a), which causes dust grains to spiral inwards towards the star, causing observable signatures such as the Zodiacal dust in the Solar System. In young late-type stars, stellar wind drag could also become significant and result in the inward migration of dust grains, similar to the effect of PR drag (P. Plavchan et al. 2005; S. G. Wolff et al. 2025). Additionally, interactions with the interstellar medium (ISM) have also been proposed to shape certain asymmetries in the distribution of small grains (D. C. Hines et al. 2007; A. Gáspár et al. 2008; G. Schneider et al. 2014).

Resolved imaging of debris disks across a range of wavelengths has provided observational constraints on the different dynamical forces in action. At mm wavelengths, observations are sensitive to thermal emission predominantly from mm-sized grains (\sim 100s of μm to cm-sized grains) which are minimally impacted by radiative forces. These observations are thought to closely trace the distribution of the planetesimals from which dust is produced, thereby mapping the parent belts that feed the collisional cascade (A. M. Hughes et al. 2018). ALMA observations have imaged dozens of these cold outer belts at tens of au and beyond (L. Matrà et al. 2025), of which two dozen have been mapped at high resolution by the ALMA survey to Resolve exoKuiper belt Substructures (ARKS, S. Marino et al. 2026), revealing substructures such as radial gaps (Y. Han et al. 2025), various vertical distributions (e.g., non-Gaussian or double-Gaussian vertical profiles, L. Matrà et al. 2019; B. Zawadzki et al. 2026) and azimuthal asymmetries (J. B. Lovell et al. 2026).

At optical and near-infrared wavelengths, observations are sensitive to micron-sized dust grains that scatter stellar radiation. These observations have revealed evidence of the radiatively displaced small grains in the form of halos, sometimes with outwardly displaced peak surface densities relative to the mm grains (J. Milli et al. 2026), possibly affected by drag forces if gas were to be present in the system (M. R. Jankovic et al. 2026; J. Olofsson et al. submitted).

More recently, JWST has offered significantly improved sensitivity and resolution for debris disk imaging in the mid-infrared over prior instruments. These wavelengths are sensitive to thermal emission from small grains in the inner tens of au of debris disks, revealing the structures of disks in these inner regions where previous instruments were not able to via emission from their micron-sized grains. Previously, *Spitzer* observations identified the presence of inner dust components in systems such as Vega (K. R. Stapelfeldt et al. 2004), Fomalhaut (K. Y. L. Su et al. 2005), and γ Oph (K. Y. L. Su et al. 2008). Around the A stars Fomalhaut and Vega, the *James Webb Space Telescope* (JWST) has recently imaged the distribution of this dust at an order of magnitude higher resolution (A. Gáspár et al. 2023; K. Y. L. Su et al. 2024). Importantly, modelling of the distribution of the warm dust component interior to the outer ALMA ring in each system has suggested that the warm dust originates from small grains migrating inwards from the parent belt via PR drag (K. Y. L. Su et al. 2024; M. Sommer et al. 2025). In the debris disk of the K star ϵ Eri, imaging by JWST's Mid-InfraRed Instrument (MIRI, G. S. Wright et al. 2023) identified inner dust consistent with stellar wind drag (S. G. Wolff et al. 2025). While weaker effects from PR drag is expected from later spectral types, this leaves the question of whether all debris disks found around early-type stars could likewise be affected by PR drag.

In light of these findings, the debris disk of γ Oph (HD 161868) offers an important point of comparison to Vega and Fomalhaut. At a distance of 29.7 pc and an age of 300 ± 200 Myr (L. Vican 2012; A. Gáspár et al. 2016; T. J. David & L. A. Hillenbrand 2015), γ Oph is of a similar spectral type (A1V) and age to Vega (A0V, 460 ± 10 Myr, J. Yoon et al. 2010) and Fomalhaut (A4V, 440 ± 40 Myr, E. E. Mamajek 2012). *Spitzer* observations at $24 \mu\text{m}$ show the disk to be highly extended, reaching 265 au (adjusted for the updated distance used here) radially (or $9''$, compared to a PSF FWHM of $6''$) or beyond (K. Y. L. Su et al. 2008). *Herschel* far-infrared observations at 70 to $160 \mu\text{m}$ spatially resolve the disc's outer belt with inner and outer edges between 50 to 300 au (N. Pawellek et al. 2014; A. Moór et al. 2015); a Gaussian belt model for the disc architecture obtains a radius of 95 au and a FWHM of 70 au (J. P. Marshall et al. 2021).

ALMA observations revealed a broad disk extending to a similar outer radius as found by *Spitzer*, with a resolved but shallow central cavity (i.e., with non-zero emission within the central cavity, S. Marino et al. 2026; Y. Han et al. 2026). Proper motion anomalies in the system suggest the possibility of undetected planets (P.

Kervella et al. 2022; J. Milli et al. 2026), but no signatures of planet-disk interactions (such as radial gaps or asymmetries) have yet been detected in the disk.

We recently imaged the debris disk of γ Oph with JWST/MIRI to test whether the PR drag scenario in Vega and Fomalhaut applies to γ Oph's radially broad belt. These images resolve the disk in the mid-infrared at more than 7 times higher resolution compared to prior imaging and form the basis of this study. We describe the observations in Section 2 and the data reduction in Section 3. We model the mid-infrared disk structure in Section 4, which we compare to ALMA observations in Section 5. Our findings are summarised in Section 6.

2. OBSERVATIONS

We observed γ Oph with the JWST MIRI Imager on 13 Aug 2024 UT (programme ID 5709, Y. Han et al. 2024). Full aperture direct images were taken with the F1500W and F2550W broadband filters. Smaller MIRI detector subarrays have higher saturation limits at the expense of a more limited field of view. To prevent saturation within each filter while still maximising the field of view to the extent possible, we employed the largest subarray that offers sufficiently fast readout speed with the FASTR1 readout pattern that avoids saturating the bright stellar core. The expected emission levels for the star and disk were determined from the spectral energy distribution (SED) of γ Oph from which the optimum subarrays were identified (the SED will be discussed in Section 5 and is shown in Fig. 5). For the F1500W and F2550W filters, this corresponded to the SUB256 and SUB128 detector subarray, respectively.

For each filter, one exposure was taken at each of 4 dither positions under the default 4-Point-Sets dithering pattern and optimised for extended sources, starting at set number 1 and proceeding for 1 set. The F1500W observations were taken with 5 groups per integration and 310 integrations per exposure, totalling 885 s of exposure time. The nominal RMS noise achieved for regions with significant disk emission as estimated by the JWST pipeline is $0.1 \mu\text{Jy}$ per pixel, with a plate scale of $0.11 \text{ arcsec}/\text{pixel}$ (or $0.03 \text{ mJy}/\text{arcsec}^2$). The F2550W observations were taken with 10 groups per integration and 45 integrations per exposure, which amounted to 592 s of exposure time. The RMS noise is $0.3 \mu\text{Jy}$ per pixel as estimated by the JWST pipeline, with the same plate scale as for F1500W ($\equiv 0.01 \text{ mJy}/\text{arcsec}^2$).

To characterise the point-spread function (PSF), subtract stellar emission and model disk emission, we also observed ζ Ser as the PSF reference star. ζ Ser is of nearly identical mid-infrared flux density to the photosphere of γ Oph (within $\sim 1\%$), thereby mitigating dif-

ferences between the science target and reference star PSF sizes that could arise due to mismatches in the flux density (I. Argyriou et al. 2023). At mid-infrared wavelengths, the impact of spectral mismatch on PSF subtraction is low. Any potential impact is further mitigated by the fact that ζ Ser (F2V) is of a sufficiently similar spectral type to γ Oph, such that no loss in sensitivity is expected even at near-infrared wavelengths, where effects of spectral type mismatches are more pronounced¹. ζ Ser has also been vetted as a single star (using the SearchCal database, A. Chelli et al. 2016, without known infrared excess). Given the faint emission of the disk around γ Oph, we also performed background observations to more accurately subtract off any background emission, which could arise from detector artefacts, even in the absence of a sky background. The background region observed was chosen to be centred at equatorial coordinates (RA, Dec) at the epoch of J2000 of (17h 47m 58.6080s, +02d 43m 24.32s) and was selected for its proximity to γ Oph and relative sparseness of background stars as suggested by *Spitzer* observations at comparable wavelengths. All PSF and background observations were carried out with identical exposure parameters as for γ Oph within the corresponding filters.

3. DATA REDUCTION

We processed the MIRI observations with the JWST pipeline version 1.18.0 using the corresponding JWST Calibration Reference Data System context `jwst_1364.pmap`. No pixels were flagged as saturated across any observations of γ Oph and ζ Ser, as expected from the observational setup (Section 2).

We first ran the default pipeline to obtain Stage 3 data products (i.e., science-ready mosaics) for the science target (γ Oph), PSF star (ζ Ser) and background observations across both filters, before performing background and PSF subtraction. However, we noticed that such a reduction results in subtle high-contrast artefacts in the PSF-subtracted image, which are likely introduced in the resampling step of the Stage 3 Imaging pipeline, when individual dithers containing both the bright stellar core and the faint disk emission are distortion corrected and aligned A. Gáspár et al. 2023; K. Y. L. Su et al. 2024.

To mitigate against these artefacts, we instead performed dither-by-dither background and PSF subtraction based on the Stage 2 pipeline products of (calibrated slope) images taken at each dither position, before combining the subtracted disk image at each dither

using the Stage 3 pipeline (K. Y. L. Su et al. 2024). Specifically, at each dither position, we subtracted the background image from the science target and reference star images taken with the corresponding filters based on the Stage 2 products. To account for slight pointing offsets between the science target and reference star at each dither, we aligned the reference star to the science target by fitting 2D Gaussians to the bright stellar cores of both, noting that the disk emission is significantly fainter than stellar emission at both wavelengths. We then subtracted a scaled version of the PSF observations from the science target to obtain the PSF-subtracted image for each dither.

We produced two versions of the PSF-subtracted imaged. The first applies PSF subtraction by scaling the reference star to the stellar component flux of the science target inferred from their SEDs, which estimates the stellar component of γ Oph to be 205 mJy at $25.5\,\mu\text{m}$ and 591 mJy at $15\,\mu\text{m}$, and ζ Ser to be 207 mJy at $25.5\,\mu\text{m}$ and 597 mJy at $15\,\mu\text{m}$ (Fig. 5 discussed in Section 5). The second version increases this scaling to further suppress any unresolved central emission and emphasise the structure of the resolved disk component without producing a negative PSF core. For this version, we increased the PSF scaling by a factor of 1.2 relative to the SED flux of γ Oph's stellar component at $25.5\,\mu\text{m}$ (equivalent to 246 mJy) and a factor of 1.04 at $15\,\mu\text{m}$ (equivalent to 615 mJy).

Although the background observations were taken with the same exposure parameters as the science target and reference star, a slight residual background remains (e.g., the F2550W observations of the science target), in some cases resulting in its background regions showing negative emission on average. We therefore corrected for the background over-subtraction by further subtracting the (negative) median background level. The reduced F2550W and F1500W images are displayed in Fig. 1.

The per-pixel RMS noise measured in the PSF-subtracted image is $0.07\,\text{mJy/arcsec}^2$ for F2550W and $0.02\,\text{mJy/arcsec}^2$ for F1500W. These noise levels are higher than those estimated by the JWST pipeline for observations of the science target alone, in part due to the fact that they carry additional uncertainties from the background and PSF observations. Within a circular aperture of $10''$ (300 au), the in-band integrated flux densities measured from the Stage 3 pipeline images (with background subtraction but without dither-by-dither PSF subtraction) are $429.55 \pm 0.06\,\text{mJy}$ at F2550W and $602.64 \pm 0.03\,\text{mJy}$ at F1500W for γ Oph, and $208.41 \pm 0.06\,\text{mJy}$ at F2550W and $550.67 \pm 0.03\,\text{mJy}$ at F1500W for ζ Ser.

¹ JWST User Documentation

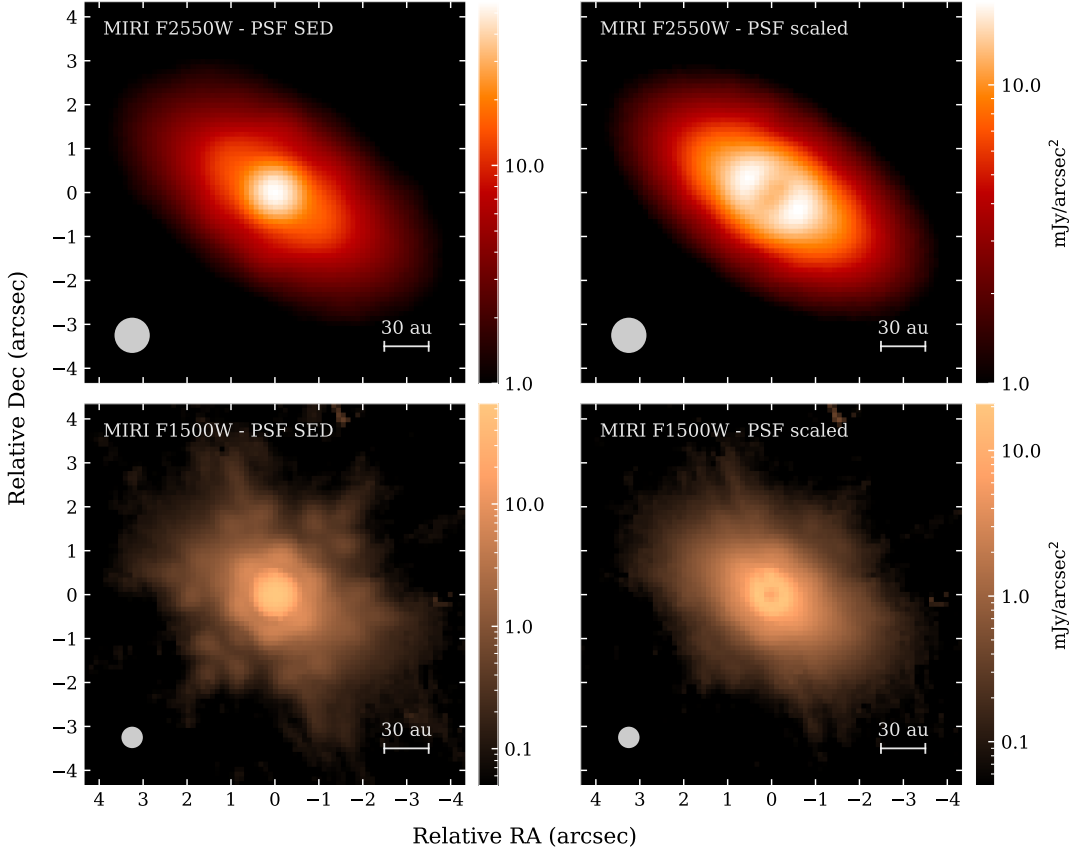


Figure 1. PSF-subtracted MIRI F2550W (top row) and F1500W (bottom row) images. The left column subtracts off a point source centred on the star scaled to the stellar flux density inferred from the SED (205 mJy for F2550W and 591 mJy for F1500W; see Section 5.3 and Fig. 5), in which the central component remains bright. The right column subtracts off a higher PSF flux density (246 mJy for F2550W and 615 mJy for F1500W) to further emphasise the structure of the resolved disk component. PSF subtraction was performed dither by dither with stage 2 products before combining the subtracted dithers with the stage 3 pipeline to produce the images displayed here. The images are displayed on a logarithmic scale. The PSF FWHM is denoted by the shaded ellipse in the bottom left corner of each panel. The orientation of the images is North up, East left.

4. RESULTS

The primary aim of this section is to characterise the spatial structure of the disk seen at mid-infrared wavelengths by experimenting with a range of models. We begin with a nonparametric approach to gauge the shape of the radial profile of the disk at $25\,\mu\text{m}$, before testing a range of parametric models in search for a satisfactory fit. We then consider the $15\,\mu\text{m}$ image in light of the $25\,\mu\text{m}$ structure that we find and attempt to recover any structural information about the disk from its significantly more centrally peaked emission.

4.1. Nonparametric modelling at $25\,\mu\text{m}$

We nonparametrically fitted the PSF-subtracted (assuming SED stellar flux) F2500W image with the `rave` package (Y. Han et al. 2022). This approach determines the deconvolved and deprojected radial surface brightness profile by fitting concentric annuli to the disk image, assuming that the disk is azimuthally symmetric and op-

tically thin. We applied the non-edge-on optimisation of the code (Y. Han et al. 2025), assuming that the vertical density distribution of the disk is Gaussian, with $\rho(z) \propto \exp[-z^2/(2h^2)]$, and that the vertical aspect ratio, $h = H(r)/r$, is constant across the disk. Note that $H(r)$ here is the standard deviation (rather than FWHM) of the vertical profile.

The application of `rave` requires an assumption on the position angle (θ) and, for the non-edge-on version of the code, the inclination (i) and vertical aspect ratio (h). Moreover, while the PSF has been subtracted assuming the SED flux of the stellar component, there could be (positive or negative) residual stellar flux and unresolved central dust emission, both of which we absorb into a central point source flux parameter (F_*) that also includes the 205 mJy already subtracted during dither-by-dither PSF subtraction. We therefore applied `rave` over a four-dimensional grid of (θ, i, F_*, h) , repeat-

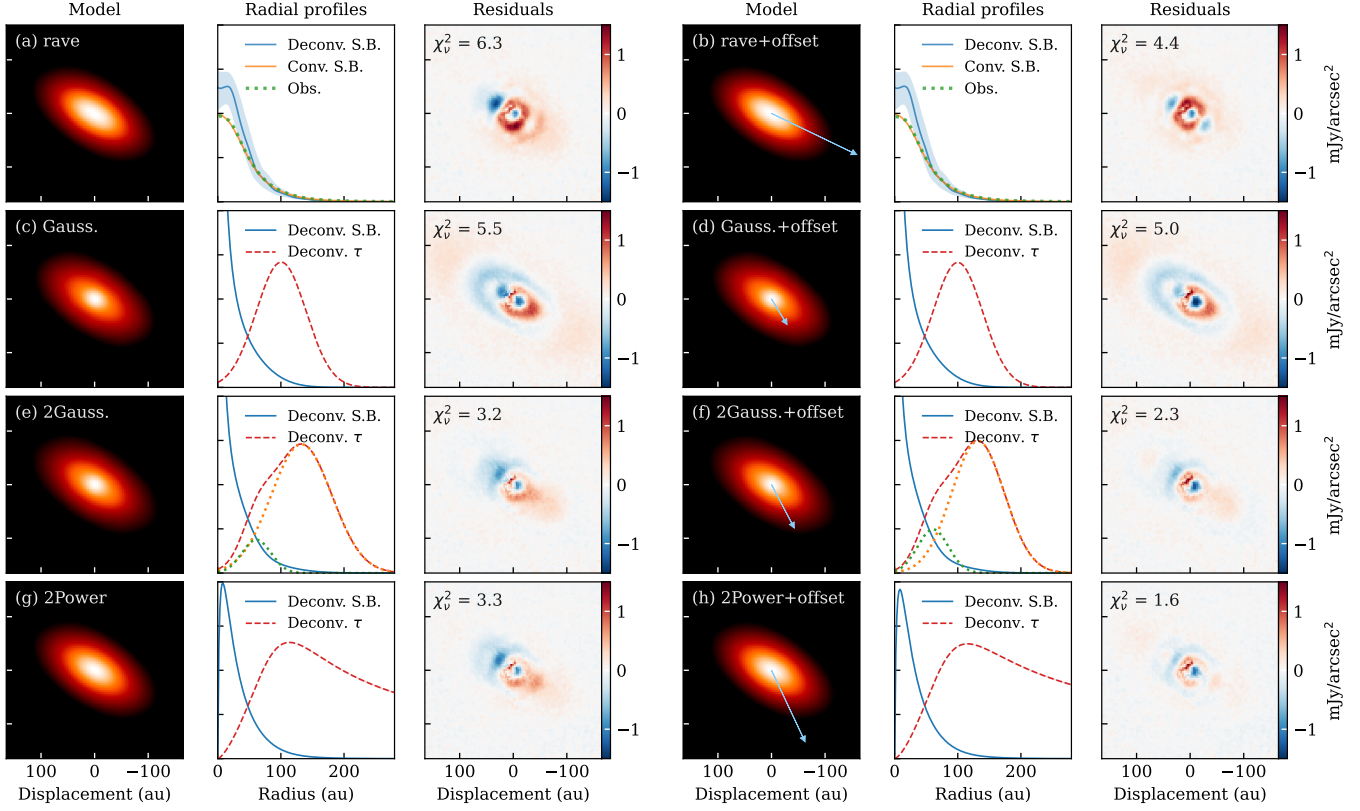


Figure 2. Gallery of nonparametric and parametric models fitted to the MIRI F2550W PSF-subtracted (assuming stellar SED flux) image of γ Oph. Each group of 3 panels displays the PSF-convolved disk-only model image (i.e., stellar component not included, displayed on a logarithmic colour scale, to be compared with the top-left panel in Fig. 1), disk-only deconvolved and deprojected radial surface brightness (S.B.) and optical depth (τ) profiles and the residual image (data – model). “Offset” indicates that the geometric centre of the disk is offset relative to the star in the model, and is included as (two) free parameters in the model. The displacement vector of the disk centre relative to the star is indicated with blue arrows. All radial profile panels are plotted with the same vertical scaling, which span from 0 to 1.8 mJy/arcsec^2 . For the `rave` radial profile panel (panel a), the azimuthally averaged profile of the PSF-subtracted (assuming the stellar flux of the best-fit grid point in the 4D `rave` grid) observations and the PSF-convolved best-fit disk model are overplotted, as this is the 1D quantity that `rave` directly fits to. Where multiple Gaussian components are invoked (panels e and f), the constituent Gaussian components are individually overplotted. Uncertainties are indicated with shaded regions for the main deconvolved profiles, but these are generally too narrow to be visible for the parametric models. The per-pixel RMS noise measured from the background is $0.07 \text{ mJy/arcsec}^2$. North is oriented upwards and east to the left.

ing the radial profile fitting procedure with 12 annuli² between 0 and 245 au from the star for each combination of the four parameters. The PSF observations were used to convolve the model. We computed the squared residuals (the sum over the squared residual image) for each median `rave` model, masking the region within $1.5''$ (45 au) from the star, which constrains significant PSF subtraction artefacts. The axes of the 4D grid were defined by the closed intervals $[57.5^\circ, 59.5^\circ]$ with 0.5° spacing for θ , $[61.0, 66.5]$ with 0.5° spacing for i and

$[230 \text{ mJy}, 250 \text{ mJy}]$ with 5 mJy spacing for F_* and the approximately logarithmically spaced sample points 0, 0.01, 0.02, 0.05, 0.1 and 0.2 for h .

We found that across the 4D grid, the best combination of parameters are $\theta = 59.0^\circ$, $I = 64.5^\circ$, $F_* = 240 \text{ mJy}$ and $h = 0.1$, as defined by the `rave` model with the lowest squared residuals. When examining each parameter individually and summing over all other axes of the grid, the four parameters each individually minimise the residuals at identical values to the best-fitting combination stated above. Note that we do not aim to estimate the uncertainties on these parameters in this section and leave this for parametric modelling in subsequent sections, which is expected to better characterise covariances between these parameters with more contin-

² Chosen based on the largest number of annuli without producing oscillatory artefacts due to noise (Y. Han et al. 2022). The surface brightness within each annulus is modelled as being constant.

uous sampling rather than a grid-based approach. Note also that any marginally resolved dust as part of the disk is likely degenerate with the central point source, preventing a robust separation of stellar and disk flux at small radii. This is further investigated with parametric models in Section 4.2 and compared with the stellar SED in Section 5. We attempt to further investigate the inner disk structure with parametric modelling in Section 4.2.

We used the `rave` profile fitted at the best-fitting grid point as the final nonparametric model. The fitted radial profile and residuals are displayed in Fig. 2a and key model assumptions are listed in Table 1.

We find that the 1D azimuthally averaged profile of the PSF-subtracted observations is well-fit by the median `rave` model as plotted in Fig. 2. However, significant residuals structures are found in the 2D residual image. While residual structures within $1''$ from the star likely correspond to PSF subtraction artefacts, which we discuss in more detail in the context of parametric modelling, extended asymmetries are seen in the resolved disk at a level of approximately 0.5 mJy/arcsec^2 relative to the symmetric `rave` model (i.e., twice of this value when comparing the two sides of the disk relative to each other). Assuming an RMS noise per pixel of $0.07 \text{ mJy/arcsec}^2$, the S/N per pixel of this asymmetry is approximately 7σ . For comparison, the disk emission at this region is approximately 9 mJy/arcsec^2 , plausibly suggesting the presence of asymmetric residual emission at the level of $\sim 5\%$. At $25 \mu\text{m}$, the star has a comparable flux to that of the total flux of the spatially extended disk, so the core of the image is thus dominated by the star and the stellar position is well-constrained by the data. This disk asymmetry about the star is thus unlikely to be due to a wrong stellar location being assumed. Removing this asymmetry requires a $\sim 1 \text{ au}$ (or 0.3 MIRI pixels) shift in the stellar location assumed, which would result in the stellar PSF appearing significantly off-centre.

To further explore the suggestion of an asymmetric disk, we repeated the `rave` fitting procedure over the 4D grid, but based on the disk image shifted by an amount that minimises its self-subtracted (i.e., disk image – disk image rotated by 180° about the star) squared residuals after PSF subtraction by F_* . We find that the optimal (θ, i, F_*, h) grid point and the values of each of the four parameters that individually minimize the squared residuals are the same as before (i.e., the case without a disk offset). The `rave` model with a stellocentric offset fitted assuming the optimal grid point is shown in Fig. 2b.

Fig. 2 and Table 1 indicate the direction and magnitude of the offset relative to the star. The magnitude of this offset is small (less than 1 au, but magnified by a factor of 100 in Fig. 2 for display), and its effect on the fitted radial profile is minor, however, the offset disk model provides improved residuals over the star-centred model, with symmetric residual structures and lower squared residuals summed over the image. We further quantify the offset with parametric modelling in Section 4.2.

4.2. Parametric modelling at $25 \mu\text{m}$

While nonparametric modelling is able to recover a versatile range of radial profile shapes, parametric modelling can yield further insights by restricting structural recovery to a few parameters of interest if a reasonably well-fitting radial profile functional form were to be assumed. Here, we begin with relatively simple functions to model the radial profile before increasing model complexity, primarily aiming to better understand the structure (e.g., radius, slope and any gaps) of the inner and outer edge of the disk.

Throughout this section, we parametrise and fit the optical depth profile (τ) rather than the surface brightness profile (S.B.), so we begin by briefly describing the conversion between the two before delving into the fitting. Converting from the optical depth to surface brightness requires assumptions on the optical properties of the emitting dust. We modelled the optical properties of dust grains using the `astrodust_optprops` code (M. Sommer et al. 2025), which calculates the absorption efficiency, $Q_{\text{abs}}(a_g, \lambda)$ (where λ is the wavelength and a_g is the grain size), the temperature profile, $T(r, a_g)$, and the ratio between radiation pressure and gravity, β , using either Mie theory, Rayleigh-Gans theory or geometric optics, depending on the grain size relative to the wavelength. The stellar luminosity was assumed to be $24.4 L_\odot$, as inferred from its SED (Fig. 5), and the mass was assumed to be $2.11 M_\odot$ (S. Marino et al. 2026).

Each dust grain was assumed to consist of a silicate core and an organic refractory mantle, with ice and voids embedded in pores (A. Li & J. M. Greenberg 1997). The optical constants of the aggregate were combined from its constituents using Maxwell-Garnett effective medium theory (C. F. Bohren & D. R. Huffman 1983). The grain composition is parametrised by a silicate fraction, q_{sil} , ice fraction, q_{ice} , and porosity, p , such that as a fraction of the total volume, $(1-p)q_{\text{sil}}$ is silicates, $(1-p)(1-q_{\text{sil}})$ is organics, $p q_{\text{ice}}$ is ice and $p(1-q_{\text{ice}})$ is voids.

Using the best-fit grain parameters fitted to MIRI observations of Fomalhaut, we assumed that the grains are

described by $q_{\text{sil}} = 0.4$, $q_{\text{ice}} = 1.0$ and $p = 0.7$ (M. Sommer et al. 2025). We further assumed that the grain size distribution follows a power law, i.e., $dN/da \propto a^{-\gamma}$, where we set $\gamma = 3.5$ expected for a steady-state collisional cascade (J. S. Dohnanyi 1969; M. C. Wyatt 2008; A. M. Hughes et al. 2018). The minimum grain size (i.e., diameter) was assumed to be $s_{\text{min}} = 15 \mu\text{m}$, which is just below the blowout size limit in the disk for this dust composition estimated to be at $17 \mu\text{m}$ (below which $\beta > 0.5$, causing fragments released from circular-orbit progenitors to be ejected from the system). The “maximum grain size” was set to be 1 m, although larger grains do not contribute significantly to the emission provided that they are much larger than the wavelength considered, which is satisfied by this choice of maximum size. The grain size distribution assumptions are consistent with previous modelling of γ Oph suggesting $\gamma = 3.6^{+0.2}_{-0.3}$ (J. P. Marshall et al. 2025b), as well as with typical observationally inferred values of γ (A. M. Hughes et al. 2018; J. P. Marshall et al. 2025b) and the expectation that s_{min} is generally found to be similar to or smaller than the blowout size for A-type stars (N. Pawellek & A. V. Krivov 2015; J. P. Marshall et al. 2025b).

4.2.1. Gaussian

We fitted a disk model assuming that the disk’s face-on optical depth is radially Gaussian, given by:

$$\tau(r) = A_1 \exp \left[-\frac{(r - \mu_{r1})^2}{2\sigma_{r1}^2} \right]. \quad (1)$$

Similar to the **rave** fitting performed, the disk was assumed to be vertically Gaussian with a vertical height aspect ratio h . In addition to A , μ_{r1} and σ_{r1} , we included θ , i , F_* and h as free parameters which we used to simulate a PSF-convolved model image to compare with the observations. Note that the observed PSF (ζ Ser) rather than a simulated PSF was used. We sampled the parameter space with a Markov chain Monte Carlo (MCMC) approach implemented with the **emcee** package (D. Foreman-Mackey et al. 2013), using 64 walkers and running the chain for at least 5,000 steps after burn-in. The noise in each pixel was assumed to be independent and Gaussian with a standard deviation equal to the rms noise described in Section 3, such that the log-likelihood function being sampled was computed as the sum of that for each pixel. Using the 16th, 50th and 84th percentiles of the marginalised posterior distribution of each parameter, we find that the model converges on the parameters displayed in Table 1.

The median model image of the disk, the fitted radial profile and the residual image are shown in Fig. 2c. Compared to the **rave** model, we find that the Gaus-

sian model lacks the wider “wing” on the outer edge that drops off more slowly towards larger radii.

To account for the misaligned geometric disk centre and stellar PSF centre, we also fitted a second version of the Gaussian model, which includes two additional free parameters that describe the spatial offset of the disk along the RA and Dec directions. Note that the stellar location is fixed in the model and aligns with the PSF centre in the data, and that only the disk component is offset relative to the star. The results of this model are shown in Fig. 2d. While residuals due to the choice of functional form of the radial profile are retained in this model as expected, the residuals are more symmetric for the version of the model with an offset, and the best-fit stellocentric offset values indicate that the offset or asymmetry of the disk is statistically significant under this choice of parametrisation.

To aid with model comparison, we computed the reduced χ^2 for each model and display these on the residual images in Fig. 2, which suggest a slightly improved model by incorporating an offset. The Akaike’s and Bayesian information criteria (AIC and BIC) are often used to evaluate the balance between the goodness of fit and the number of free parameters. As we have assumed each of the $\sim 10^4$ pixels to be an independent data point, even small improvements in the reduced χ^2 (e.g., by 0.1) causes the log-likelihood term in the AIC or BIC to dominate over the penalty term which only varies by a few free parameters. Indeed within the scope of this study, the AIC and BIC preference is always consistent with the model with the lower reduced χ^2 , hence for simplicity throughout this section we base the comparison directly on the reduced χ^2 .

4.2.2. Two Gaussians

To account for the broad “wings” on the outer edge that the Gaussian model residuals suggest, we fitted a more complex model with two Gaussian radial components, with the optical depth given by:

$$\tau(r) = A_1 \exp \left[-\frac{(r - \mu_{r1})^2}{2\sigma_{r1}^2} \right] + A_2 \exp \left[-\frac{(r - \mu_{r2})^2}{2\sigma_{r2}^2} \right]. \quad (2)$$

The best-fit double-Gaussian model is shown in Figs. 2e and f, with the corresponding fitted parameters displayed in Table 1. This model shows less prominent residual disk structures than the ring-like residuals seen in the single-Gaussian models. The residual features are more similar to the star-centred **rave** model, although at a lower amplitude and with a lower χ^2_ν .

To reduce the asymmetry of the residuals, we also tested a double-Gaussian model with a stellocentric offset, which indeed further improves the fit. The best-fit

Table 1. Assumed parameters for rawe and fitted values for parametric models at $25\mu\text{m}$.

Parameter	rawe		Gaussian		Two Gaussians		Two power laws	
	No offset	Offset	No offset	Offset	No offset	Offset	No offset	Offset
F_* (mJy)	240	240	$220.68^{+0.05}_{-0.05}$	$220.98^{+0.05}_{-0.05}$	$226.5^{+0.2}_{-0.2}$	$229.30^{+0.08}_{-0.08}$	$235.78^{+0.04}_{-0.04}$	$236.32^{+0.04}_{-0.04}$
A_1			$1.034^{+0.001}_{-0.001} \times 10^{-4}$	$1.031^{+0.003}_{-0.001} \times 10^{-4}$	$1.063^{+0.003}_{-0.003} \times 10^{-4}$	$1.089^{+0.003}_{-0.003} \times 10^{-4}$	$1.337^{+0.003}_{-0.003} \times 10^{-4}$	$1.300^{+0.003}_{-0.003} \times 10^{-4}$
μ_{r1} (au)			$100.48^{+0.10}_{-0.09}$	$99.99^{+0.09}_{-0.10}$	$132.7^{+0.6}_{-0.6}$	$132.0^{+0.4}_{-0.4}$		
σ_{r1} (au)			$39.53^{+0.04}_{-0.04}$	$39.27^{+0.04}_{-0.04}$	$48.0^{+0.3}_{-0.3}$	$41.8^{+0.2}_{-0.2}$		
A_2					$2.75^{+0.10}_{-0.09} \times 10^{-5}$	$3.61^{+0.05}_{-0.05}$		
μ_{r2} (au)					$61.3^{+0.4}_{-0.4}$	$60.8^{+0.3}_{-0.3}$		
σ_{r2} (au)					$22.8^{+0.4}_{-0.4}$	$24.4^{+0.1}_{-0.1}$		
R_c (au)							$102.4^{+0.3}_{-0.3}$	$98.0^{+0.3}_{-0.3}$
α_{in}							$1.443^{+0.002}_{-0.002}$	$1.472^{+0.002}_{-0.002}$
α_{out}							$-0.89^{+0.02}_{-0.02}$	$-0.72^{+0.02}_{-0.02}$
i (deg)	64.5	64.5	$62.94^{+0.02}_{-0.02}$	$62.93^{+0.02}_{-0.02}$	$63.30^{+0.02}_{-0.02}$	$63.28^{+0.02}_{-0.02}$	$63.30^{+0.02}_{-0.02}$	$63.29^{+0.02}_{-0.02}$
θ (deg)	59.0	59.0	$58.81^{+0.02}_{-0.02}$	$58.81^{+0.02}_{-0.02}$	$58.82^{+0.02}_{-0.02}$	$58.84^{+0.02}_{-0.02}$	$58.82^{+0.02}_{-0.02}$	$58.83^{+0.02}_{-0.02}$
h	0.1	0.1	$0.1045^{+0.0009}_{-0.0009}$	$0.1064^{+0.0009}_{-0.0009}$	$0.0223^{+0.0007}_{-0.0006}$	$0.0226^{+0.0008}_{-0.0008}$	$0.0222^{+0.0006}_{-0.0006}$	$0.0227^{+0.0006}_{-0.0006}$
Δ_{RA} (au)			-0.46	$-0.239^{+0.005}_{-0.005}$		$-0.379^{+0.006}_{-0.006}$	$-0.584^{+0.007}_{-0.007}$	
Δ_{Dec} (au)			-0.22	$-0.390^{+0.007}_{-0.007}$		$-0.721^{+0.009}_{-0.009}$	$-1.24^{+0.01}_{-0.01}$	

Table 2. Assumed (*) and fitted values for parametric models at $15\mu\text{m}$.

Parameter	Gaussian	
	No offset	Offset
F_* (mJy)	$614.1^{+0.2}_{-0.2}$	$615.2^{+0.2}_{-0.2}$
A_1	$2.19^{+0.02}_{-0.02} \times 10^{-4}$	$2.16^{+0.02}_{-0.02} \times 10^{-4}$
μ_{r1} (au)	$100.4^{+0.5}_{-0.5}$	$99.4^{+0.5}_{-0.5}$
σ_{r1} (au)	$33.4^{+0.2}_{-0.2}$	$33.1^{+0.2}_{-0.2}$
i (deg)	63*	63*
θ (deg)	59*	59*
h	0.11*	0.11*
Δ_{RA} (au)		$0.421^{+0.010}_{-0.009}$
Δ_{Dec} (au)		$-0.77^{+0.01}_{-0.01}$

star-disk offset is oriented along the same direction as the single-Gaussian model, with a slightly larger amplitude.

4.2.3. Power law edges

To test a simple model capable of producing inner and outer edges with different slopes, we parameterised the optical depth of the edges as power laws with different exponents. We used the double-power-law parametrisation from [Y. Han et al. \(2025\)](#), given by:

$$\tau(r) = \frac{A_1}{\sqrt{(r/R_c)^{-2\alpha_{\text{in}}} + (r/R_c)^{-2\alpha_{\text{out}}}}}, \quad (3)$$

which introduces a smooth transition where the two edges meet near the peak. We fitted a model both with and without a stellocentric offset. The results are shown in Table 1 and visualised in Figs. 2g and h.

Similar to the previous models, introducing a star-disk offset noticeably improves the symmetry of the residuals and produced the lowest reduced χ^2 among all models that we fitted to the F2550W image. The residual features near the star show an oscillatory pattern between narrow positive and negative annuli, which is likely due to imperfections in PSF subtraction despite the relatively high PSF stability of JWST, rather than real dust features. Note that while the reduced χ^2 of 1.6 is still greater than 1, this includes the effects of imperfect PSF subtraction near the star. We adopt this power-law model with a disk offset as the best-fitting parametric model at $25\mu\text{m}$.

4.3. Parametric modelling at $15\mu\text{m}$

The significantly more compact emission and higher star-disk contrast at $15\mu\text{m}$ compared to $25\mu\text{m}$ makes it difficult to fit a meaningful nonparametric model at $15\mu\text{m}$ that attempts to deconvolve marginally resolved

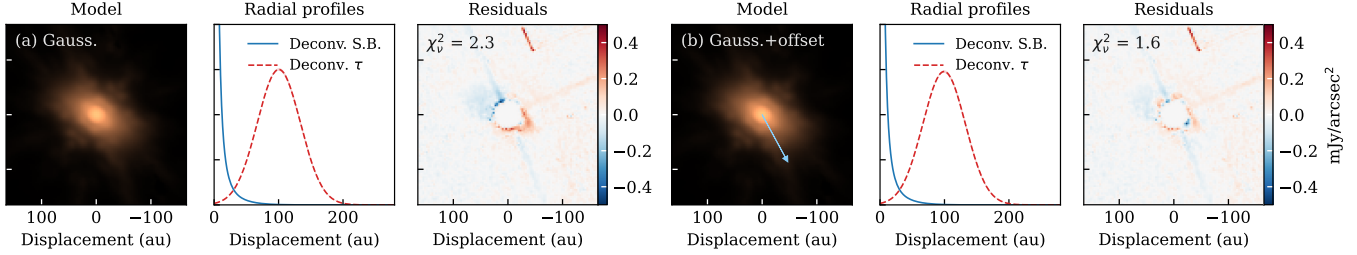


Figure 3. Gaussian model fitted to the MIRI F1500W image of γ Oph. The panels are the same as those described in Fig. 2 for the F2550W modelling and the model image should be compared with the bottom-right panel of Fig. 1. The central region has been masked as it is dominated by PSF subtraction artefacts and was not used for model fitting. The per-pixel RMS noise measured from the image background is $0.02 \text{ mJy/arcsec}^2$.

disk emission from the bright PSF core. Even given the PSF stability of JWST, PSF uncertainties produce PSF subtraction artefacts that make even parametric fitting challenging. Nonetheless, we attempted to fit a simple model with a restricted set of free parameters to extract basic structural information about the disk at this wavelength.

We attempted to fit a Gaussian model analogous to that fitted to the F2550W image as described in Section 4.2.1, however the model did not converge to a single solution as parameters such as i , θ and h become degenerate with the radial profile given the relatively compact and faint emission relative to imaging artefacts. We therefore restricted the model by fixing the i , θ and h parameters based on the best-fit values of the $25 \mu\text{m}$ Gaussian disk model, fitting only to F_* , A_1 , μ_{r1} and σ_{r1} (Eq. (1)). We also masked out the central 33 au (i.e., 10 MIRI pixels) where PSF subtraction artefacts are most prominent. The best-fit parameters of this model are shown in Table 2, and the fitted model image, radial profile and residuals are shown in Fig. 3a.

This restricted Gaussian model is broadly able to account for the disk emission at $15 \mu\text{m}$, though asymmetric residual structures exist. These residuals are significantly reduced with the introduction of a star–disk offset as shown in Fig. 3b, with the best-fit offset comparable to those found at $25 \mu\text{m}$. While many of the residual features are imaging artefacts, there appear to be subtle residual emission that align with the orientation of the disk.

5. DISCUSSION

We compare γ Oph observations across wavelength in this section and begin by pointing out two pieces of information referenced throughout the discussion. Firstly, ALMA observations of γ Oph have been taken as part of the REASONS sample (L. Matrà et al. 2025), and more recently as part of the ARKS programme (S. Marino et al. 2026). Here we focus on the latter, which were carried out in Band 7 (0.87 mm) at higher resolution

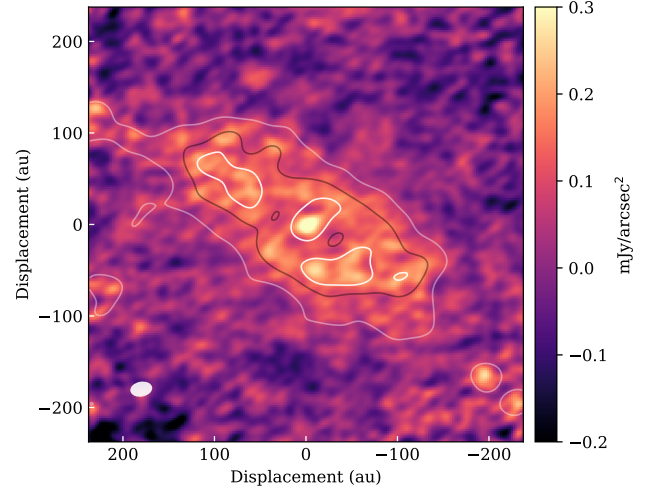


Figure 4. ALMA Band 7 observations presented in S. Marino et al. (2026), imaged with `clean` using a robust parameter of 2.0 and with primary beam correction applied. The beam FWHM is indicated with a white ellipse in the bottom-left corner. Contours are drawn at 0.06 , 0.12 and $0.15 \text{ mJy arcsec}^{-2}$ based on the image smoothed with a 1 arcsec UV taper.

(15 au) than the REASONS observations. A `clean` image of the ALMA observations is shown in Fig. 4. Secondly, we assembled the SED of γ Oph, which is shown in Fig. 5. Specific data points and stellar models used are described in the legend of the SED.

5.1. Mid-infrared disk structure

The modelling approaches in Section 4 together support four main conclusions on the disk morphology in the mid-infrared.

Firstly, the outer edge of the disk exhibits a smooth drop-off with no evidence for radial gaps or additional rings based on the MIRI dataset. The optical depth (or surface density) profile appears to be shallower at the outer edge than the inner edge, as suggested by the better fit of the power-law-edges model compared to the radially symmetric Gaussian model. The deconvolved

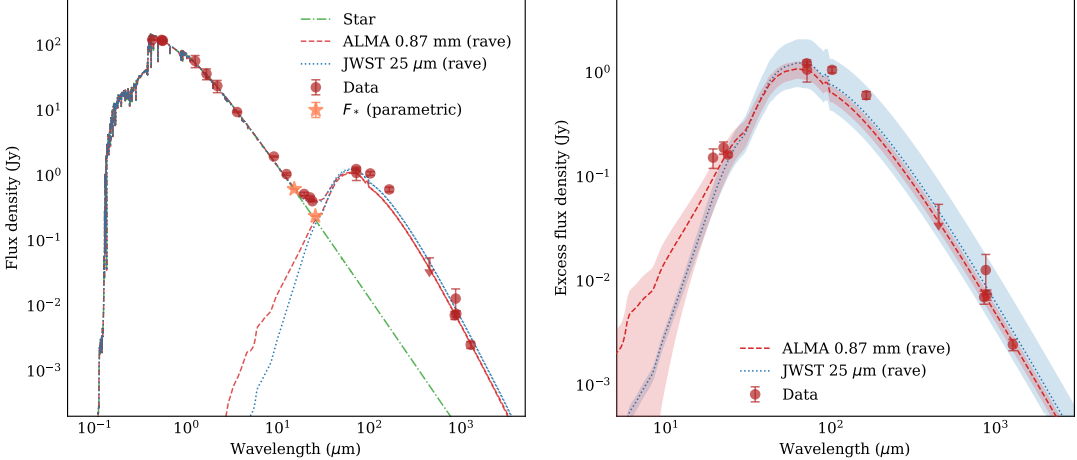


Figure 5. The SED of γ Oph. The photometric data points were collected from *Hipparcos* (ESA 1997; E. Høg et al. 2000), the J. C. Mermilliod (2006) UBV catalogue, 2MASS (R. M. Cutri et al. 2003), *Gaia* (Gaia Collaboration et al. 2018), AKARI (D. Ishihara et al. 2010), WISE (E. L. Wright et al. 2010), *Spitzer* (K. Y. L. Su et al. 2006; C. H. Chen et al. 2014; IRSA & SSC 2020), *Herschel* (G. L. Pilbratt et al. 2010; N. Pawellek et al. 2014; A. Moór et al. 2015), JCMT (W. S. Holland et al. 2017), APEX (R. Nilsson et al. 2010) and ALMA (L. Matrà et al. 2025; S. Marino et al. 2026). The F_* points represent the fitted central component flux under then double-power-law-with-offset model at $25\mu\text{m}$ and the Gaussian-with-offset model at $15\mu\text{m}$. The stellar spectrum corresponds to a Phoenix stellar model (T. O. Husser et al. 2013) with $T_{\text{eff}} = 9050\text{ K}$ and $\log(g) = 3.9$. The SED models of the disk are overplotted, including those derived using `rave` on the ALMA 0.87 mm and JWST 25 μm images, both with the same grain composition and size distribution as described in Section 4.2.

radial profile obtained with `rave` drops to 0 upon reaching 250 au, which is consistent with the furthest emission detected in the azimuthally averaged radial profile measured directly from the (PSF-convolved) observations (see Appendix A). This MIRI $25.5\mu\text{m}$ disk extent is therefore similar to the 260 au lower limit of the disk radius inferred from *Spitzer* observations at $24\mu\text{m}$ (K. Y. L. Su et al. 2008). Note that the *Spitzer* observations reached a per-pixel RMS noise of $0.9\mu\text{Jy}/\text{arcsec}^2$ for its $2''.55$ MIPS24 pixels. The MIRI F2550W RMS noise achieved here corresponds to $3\mu\text{Jy}/\text{arcsec}^2$ per *Spitzer* MIPS24 pixel (binning MIRI pixels and adding noise in quadrature), which is comparable but slightly noisier than the *Spitzer* observations accounting for differences in the central wavelength. At $15\mu\text{m}$, the outermost dust detected is at approximately 150 au from the star based on the azimuthally averaged radial profile of the (convolved) observations (Fig. 9).

Secondly, the MIRI images do not directly resolve an inner disk cavity in surface brightness, though the presence of an inner edge in the underlying optical depth/surface density is inferred from the surface brightness profiles derived. The disk and central component flux (i.e., stellar flux + any unresolved inner disk emission) from nonparametric modelling are plotted on the SED of the system shown in Fig. 5. The relative consistency between the predicted stellar spectrum and the fitted central point source flux suggests that despite an inner edge not being resolved, the level of emission con-

tributed by any unresolved inner dust is low compared to the stellar flux.

Thirdly, the disk appears to be asymmetric, and can be modelled by an axisymmetric disk with a geometric centre offset from the star. It is possible that the asymmetry could alternatively be modelled by a geometrically axisymmetric disk centred on the star but with azimuthally asymmetric emission, or a combination of the two scenarios in a more physically realistic model such as due to a nonzero eccentricity (M. C. Wyatt 2005b; J. B. Lovell et al. 2021; E. M. Lynch & J. B. Lovell 2022; J. B. Lovell & E. M. Lynch 2023), but these models are not tested in this study. Taking the stellocentric offset values from the power-law-edges model, which offered the best fit, the projected offset from the star is 1.371 ± 0.009 au along $205.2 \pm 0.3^\circ$ counterclockwise from north (for comparison, the major axis position angle is 58.7°), corresponding to a 2.04 ± 0.02 au offset along $-55.9 \pm 0.3^\circ$ counterclockwise from the ascending (western) node when deprojected given the fitted inclination and position angle of the disk. Assuming a semimajor axis of 50 au where the asymmetry in the axisymmetric model residuals peak, such an offset corresponds to an eccentricity of ~ 0.02 . ALMA observations of γ Oph did not identify any asymmetries in the disk (S. Marino et al. 2026; J. B. Lovell et al. 2026). However, an asymmetry at the same level as that seen by JWST would not have been detectable in the ALMA images, as the disk at peak emission is only detected at 6σ in these ob-

servations. Future deeper ALMA observations may be able to search for evidence of the subtle asymmetry that we find here.

Finally, based on the models with an axisymmetric disk with a stellocentric offset, the vertical aspect ratio seen by MIRI appears to be large (~ 0.1) based on nonparametric modelling, however the values of h returned by parametric modelling ranges widely between 0.02 and 0.11 depending on the choice of parametrisation, suggesting that the aspect ratio is in practice not tightly constrained. For comparison, the best-fit aspect ratios measured with ALMA generally range between 0.13 and 0.16 (J. Terrill et al. 2023; L. Matrà et al. 2025; Y. Han et al. 2025; B. Zawadzki et al. 2026), and this range expands to be 0.08 to 0.18 when considering the uncertainties of individual measurements. An exception to this general range is an upper limit of 0.08 placed using the `frank` code (J. Jennings et al. 2020; J. Terrill et al. 2023) based on the ARKS dataset (S. Marino et al. 2026).

If the mid-infrared aspect ratio were to be 0.13, we estimate that at a radius of 100 au where the disk's optical depth peaks (see Section 5.3 and Fig. 8), this corresponds to a deprojected vertical standard deviation of $0.4''$, or a deprojected vertical FWHM approximately 30% larger than the PSF FWHM. An aspect ratio of 0.13 or larger would then be measurable in theory given the high sensitivity of the MIRI observations, even when taking into account projection effects given the $\sim 60^\circ$ inclination of the disk. The fact that all MIRI models prefer an aspect ratio below this value could suggest that the MIRI aspect ratio is lower than, or near the lower end of, the likely scale height range measured from ALMA. However, the MIRI models prefer a lower (more face-on) inclination than the ALMA models, which could bias the MIRI models towards a lower scale height, so without further joint modelling, it is difficult to draw a robust comparison. A MIRI scale height smaller than ALMA would be consistent with that suggested in AU Mic by comparing ALMA observations at different bands (D. Vizgan et al. 2022), which is consistent with predictions of smaller inclination dispersions among smaller grains from collisional damping (M. Pan & H. E. Schlichting 2012). However, studies have also suggested that the efficiency of collisional damping and its effect on the scale height could be limited (J. P. Marshall et al. 2023; M. R. Jankovic et al. 2024; J. P. Marshall et al. 2025a).

5.2. Planet constraints

Since the presence of sufficiently massive planets in the disk is expected to carve resolvable gaps within the age

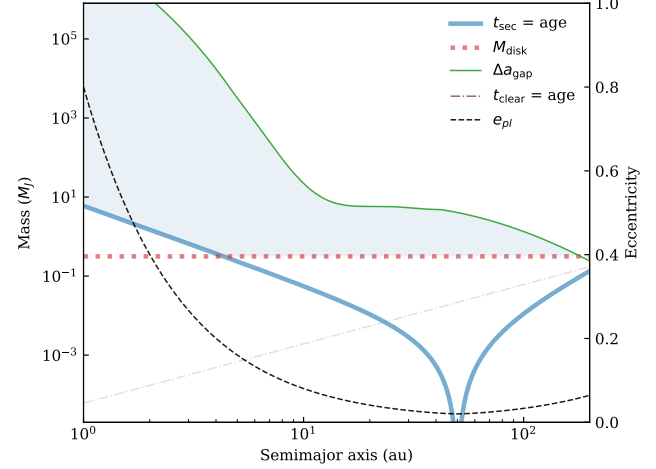


Figure 6. Constraints on the mass (left axis), eccentricity (right axis) and semimajor axis of a hypothetical planet required to explain the stellocentric offset of the disk. Lower bounds in the mass–semimajor axis parameter space are plotted with thick lines and upper bounds with thin lines. Origins of lower bounds include a sufficiently fast secular perturbation timescale such that the disk becomes eccentric within the age of the system ($t_{\text{sec}} = \text{age}$), and a sufficiently massive planet to overcome the disk's gravity (M_{disk}). Upper bounds are set by the lack of a radial gap detected in MIRI observations, either due to the gap being too narrow (Δa_{gap}), or due to a gap having not yet been carved by the planet within the age of the system ($t_{\text{clear}} = \text{age}$). The shaded region simultaneously satisfies all such constraints described. The eccentricity required of the planet to excite a forced eccentricity of 0.02 in the disk at 50 au is overplotted on a separate vertical axis with a black dashed line (e).

of the system, the lack of gaps resolved by MIRI places upper limits on the mass of any planets that could reside within the disk.

A planet could hide within the disk if any radial gap that it carves is too narrow to be detected. For a planet on a circular orbit, we estimated the width of gaps carved by the chaotic overlap of first order mean-motion resonances as:

$$\Delta a \approx 3a_{\text{pl}} \left(\frac{M_{\text{pl}}}{M_*} \right)^{2/7}, \quad (4)$$

i.e., the chaotic zone combined from both sides of the planet (J. Wisdom 1980; S. Morrison & R. Malhotra 2015), where a_{pl} is the semimajor axis of the planet, M_{pl} is the mass of the planet and M_* is the mass of the star, which is inferred to be $2.11 M_\odot$ for γ Oph (S. Marino et al. 2026).

To test the widest gap that could hide in the disk while remaining undetected, we simulated observations using the `rave` radial profile derived in Section 4 and added a Gaussian gap that is fully cleared at the local

minimum within the gap. The maximum undetectable gap width depends on the radius at which the gap is centred, which we find ranges from a quarter of a PSF FWHM for a gap at 10 au, to half at 25 au, to a full PSF above 75 au (due to the emission being too faint) or less than 5 au (due to the PSF core). For reference, the PSF FWHM is 24 au. We interpolated between sample points of the maximum undetectable gap width as a function of semimajor axis and plot the smoothed constraints from Eq. (4) in Fig. 6. The deviation of the curve from a straight line reflects the higher sensitivity to fully cleared gaps at intermediate semimajor axes.

A second way in which a planet in the disk could avoid leaving a detectable gap is if the gap-clearing timescale is longer than the age of the system. Following A. Shannon et al. (2016), the timescale required to clear the gap can be estimated as:

$$t_{\text{clear}} \approx 4 \text{ Myr} (M_{\text{pl}}/M_{\oplus})^{-1} (a_{\text{pl}}/\text{au})^{3/2} (M_{*}/M_{\odot})^{1/2}. \quad (5)$$

This is plotted in Fig. 6 assuming an age of 300 Myr, which shows that any planet capable of eventually carving a gap wide enough for detection can do so within a short enough timescale, such that the effective upper limit is set by the Δa rather than t_{clear} constraint.

If the stellocentric offset of the disk is due to a forced eccentricity of 0.02 (see Section 5.1) that is imposed by an eccentric planet, the secular timescale is required to be shorter than the age of the system, placing a lower limit on the perturbing planet's mass. We estimated the secular timescale (C. D. Murray & S. F. Dermott 1999; M. C. Wyatt 2005a; A. A. Sefilian et al. 2021) via

$$t_{\text{sec}} = 2\pi \left[\frac{1}{4} n \frac{M_{\text{pl}}}{M_{*}} \alpha \bar{\alpha} b_{3/2}^1(\alpha) \right]^{-1}, \quad (6)$$

where $\alpha = \min(a_{\text{disk}}, a_{\text{pl}})/\max(a_{\text{disk}}, a_{\text{pl}})$, $n = \sqrt{G(M_{*} + M_{\text{pl}})/a_{\text{disk}}^3}$, $\bar{\alpha} = \min(1, a_{\text{disk}}/a_{\text{pl}})$, $b_s^m(\alpha)$ are the standard Laplace coefficients, and we set $a_{\text{disk}} = 50$ au where the surface brightness asymmetry peaks. This condition is plotted in Fig. 6.

Furthermore, the planet would also need to be larger than the disk mass to dominate over the disk's self-gravity (A. A. Sefilian 2024; A. A. Sefilian et al. 2025), otherwise secular resonances would have led to gapped structures which we don't find (A. A. Sefilian et al. 2021, 2023)³. There is considerable uncertainty surrounding the total mass of debris disks, although interpolations of

³ The threshold planet mass to overcome the disk's self-gravity in principle depends on the planet's semimajor axis and the disk's surface density profile (A. A. Sefilian 2024), but we ignore this dependence here and only show an indicative threshold given that the disk mass itself is highly uncertain.

the collisional cascade from dust to planetesimals suggest values above tens of M_{\oplus} (A. V. Krivov & M. C. Wyatt 2021). In Fig. 6, we plot an indicative disk mass of $100 M_{\oplus}$ based on the lower end of disk masses interpolated from a collisional cascade that is also within the estimated gravitational stability limit during planet formation (A. V. Krivov & M. C. Wyatt 2021).

In addition to the mass, we can also constrain the eccentricity required of a perturbing planet. Assuming a disk forced eccentricity of $e_{\text{f}} = 0.02$ as before at a peak surface brightness asymmetry of $a_{\text{disk}} = 50$ au, we estimated the required perturber's eccentricity via

$$e_{\text{pl}} = \frac{b_{3/2}^1(\alpha)}{b_{3/2}^2(\alpha)} e_{\text{f}} \quad (7)$$

(M. C. Wyatt et al. 1999; A. A. Sefilian et al. 2021). This eccentricity condition is plotted in Fig. 6 on a separate vertical axis from the mass axis. Note that Eq. (7) is valid for massless disks; the inclusion of disk gravity modifies the forced eccentricity, both in terms of its amplitude and radial dependence (A. A. Sefilian 2024).

The intersection of the MIRI mass–semimajor axis constraints is shown with the shaded region in Fig. 6. The strongest constraints are primarily set by the maximum hidden gap width, which permit giant planets up to $10 M_{\text{Jup}}$ to reside outside 10 au, with an eccentricity required to be a few percent to induce the disk asymmetry due to secular perturbation. Such a scenario is possible even if the disk is as massive as assumed. If the perturber were to reside within 10 au, the mass threshold becomes significantly larger and a brown dwarf or close binary companion could remain hidden while perturbing the disk. Such a perturber is compatible with proper motion anomalies of γ Oph that have led to a prediction of a $9\text{--}100 M_{\text{Jup}}$ planet at 3–25 au (P. Kervella et al. 2022; J. Milli et al. 2026), which overlaps with the allowable mass range based on MIRI for semimajor axes under 10 au.

5.3. Disk structure across wavelength

The aim of this section is to compare the radial structure of the disk across wavelength, particularly between JWST and ALMA. Specifically, we compare the MIRI radial profile fitted nonparametrically with `rave` with those fitted using the same method to the ARKS ALMA observations (Fig. 4). We also include the ALMA nonparametric profile fitted with the `frank` method (J. Jennings et al. 2020; J. Terrill et al. 2023) in this comparison, which fits directly to ALMA visibilities (rather than the CLEAN image as in the case of `rave`). The ALMA profiles are fitted to star-subtracted observations assum-

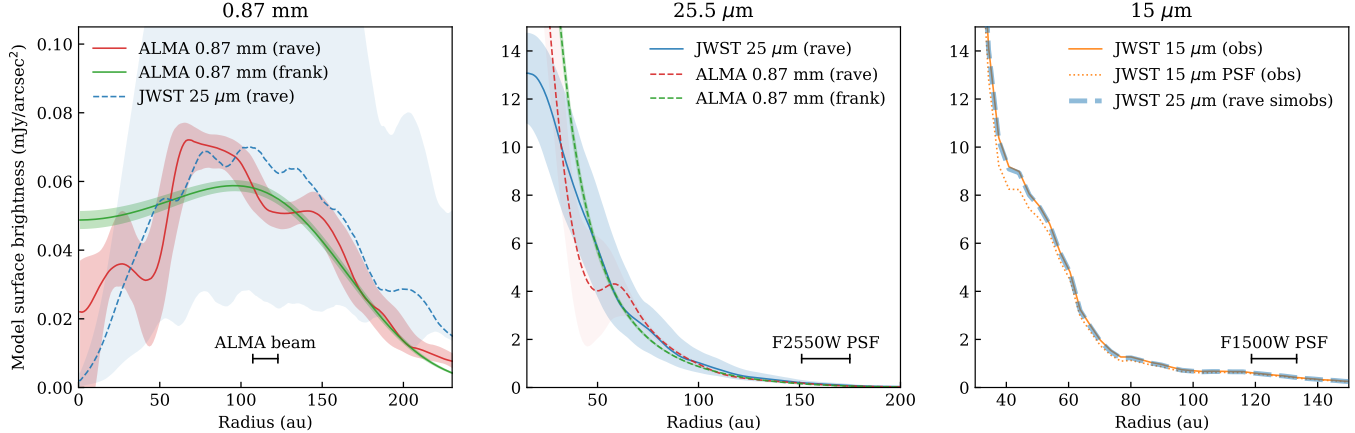


Figure 7. Radial surface brightness profiles at the ALMA Band 7 (left), MIRI F2550W (middle) and MIRI F1500W (right) wavelengths. Solid lines indicate deconvolved and deprojected disk-only (i.e., star-subtracted) profiles fitted directly to observations at the corresponding wavelength, with an exception being the F1500W profile, which is the PSF-convolved profile measured directly by azimuthally averaging the (star-included) observations given the difficulty in robustly deconvolving the compact disk emission. Dashed profiles indicate those converted from observations at other wavelengths assuming a spatially uniform grain size distribution and grain composition as described in Section 4.2. In the right panel which displays 15 μm profiles, the dotted line indicates the azimuthally averaged profile of the PSF, which is scaled to a flux density of 0.64 Jy. The dash-dotted line is the sum of the azimuthally-averaged PSF-convolved disk model and the aforementioned dotted line corresponding to the PSF.

ing a stellar flux of 0.161 mJy. Details of the ALMA modelling are described in Y. Han et al. (2026).

5.3.1. Collisional cascade

Fig. 7 displays the surface brightness profiles at 25 μm and 0.87 mm. The ALMA observations resolve an inner edge and central cavity, although the exact distribution at the inner edge is somewhat uncertain, as demonstrated by the different radial profile shapes recovered by `rave` and `frank`. It should be pointed out that the “wiggles” in the ALMA `rave` profile likely reflect noise in the image, as the ALMA observations reach a lower S/N than the MIRI observations. Note that the ALMA beam size is slightly smaller than the MIRI F2550W PSF (by $\sim 1/3$), as indicated in Fig. 2. The ALMA position angle is measured to be $57.6 \pm 1.6^\circ$ and the inclination $66.1 \pm 1.5^\circ$ by fitting a Gaussian ring model (S. Marino et al. 2026). This is consistent with the MIRI position angle of $58.83 \pm 0.02^\circ$ and slightly larger than the inclination of $63.29 \pm 0.02^\circ$ determined from the power-law-edges-with-offset model.

To compare these observations, we convert the surface brightness profiles between wavelength assuming the same optical properties as those described in Section 4.2. We find that a steady-state collisional cascade with $\gamma = 3.5$ (J. S. Dohnanyi 1969; M. C. Wyatt 2008; A. M. Hughes et al. 2018) and a minimum grain size of 15 μm is consistent with the 25 μm and 0.87 mm surface brightness profiles that we observe. The surface brightness profile converted between wavelength assuming a common underlying surface density profile are overplot-

ted in Fig. 7. No vertical scaling is applied between profiles within each panel. While deviations exist at <50 au in the 25 μm panel, this is likely a reflection of degeneracies between disk emission at small radii and any unresolved central component, since even a small nonzero flux in the ALMA radial profile becomes significantly magnified when converted to 25 μm . Similarly, the large uncertainties of the MIRI 25 μm profile in the 0.87 mm panel reflects the large fractional uncertainties in the region with low-amplitude emission in the MIRI observations.

While the deconvolved radial profile is difficult to determine at 15 μm due to the compact and faint emission, we converted the 25 μm radial profile to 15 μm assuming the same optical properties as described above. We convolved the resulting model image with the F1500W PSF to derive the azimuthally averaged surface brightness profile, which we find is consistent with the same quantity measured from the observations.

Furthermore, we modelled the SED of the disk assuming either the 25 μm or 0.87 mm `rave` profiles, as shown in Fig. 5, which is broadly consistent with available infrared to mm photometry. Radially extended halos have been linked to small grains displaced from the parent planetesimal belt due to processes such as radiation pressure in debris disk systems such as Vega (K. Y. L. Su et al. 2005), β Pic (N. P. Ballering et al. 2016) and HD 32297 (J. Olofsson et al. 2022). Although such a process could still occur in radially extended belts (P. Thébault & J.-C. Augereau 2007), the multi-wavelength analysis suggests that despite the large ra-

dial extent of γ Oph observed at mid-infrared and mm wavelengths is consistent with a common grain size distribution throughout the disk, as expected for a disk populated by a radially extended planetesimal belt undergoing steady-state collisions.

To further visualise the consistency of the observations with a uniform size distribution, we plot in Fig. 8 the geometric optical depth profiles derived from both JWST and ALMA under the steady-state grain size distribution with $\gamma = 3.5$. These nonparametric profiles show a high degree of consistency without the need to introduce any vertical scaling.

5.3.2. Inner and outer edges

For a disk evolving under steady-state collisions without truncating planets, the inner edge is expected to scale as $r^{7/3}$ (G. M. Kennedy & M. C. Wyatt 2010). Such a profile is consistent with the inner edge of JWST and ALMA `rave` profiles within uncertainties, as shown in Fig. 8. However, observational constraints on the steepness of the inner edge carry relatively large uncertainties, and ALMA parametric fitting that model the radial profile with a power-law inner and outer edge find a shallower inner edge with an exponent of 1.0 ± 0.1 (Y. Han et al. 2026).

While we have shown that there exists a steady-state grain size distribution that consistently explains the observations, given the steep emission dropoff as function of radius at MIRI wavelengths, large fractional uncertainties associated with the faint outer disk in the translate to uncertain optical depth profiles in the outer edge, and we are unable to place more stringent constraints on the level of any halo emission in Fig. 9 based on the nonparametric `rave` profile.

Note also that the minimum grain size of $15\,\mu\text{m}$ assumed in our model is slightly smaller than the $17\,\mu\text{m}$ radiation pressure blowout size estimated from the optical properties assumed. The minimum grain size in debris disks has been found to be on average similar to the expected blowout size around A stars N. Pawellek et al. (2014), however more recent analyses with a larger sample have found that for early A stars, the minimum grain size is on average smaller than the blowout size (J. P. Marshall et al. 2025b), as unbound sub-blowout grains could still contribute to dust emission (P. Thébault & Q. Kral 2019). Furthermore, small deviations are expected as our models of the optical properties of dust are imperfect, and the truncated power-law grain size distribution is an approximation of the true grain size distribution (P. Thébault & J.-C. Augereau 2007).

5.3.3. Warm inner dust

The presence of warm dust interior to ALMA-imaged belts has been a notable finding from debris disk imaging with MIRI so far (A. Gáspár et al. 2023; K. Y. L. Su et al. 2024). While γ Oph adds to the growing list of debris disks showing well-resolved inner dust emission absent from ALMA observations, the interpretation for γ Oph based on our findings appears to differ somewhat from Fomalhaut (A. Gáspár et al. 2023) and Vega (K. Y. L. Su et al. 2024).

In the case of Fomalhaut and Vega, the ALMA observations suggest a relatively sharp inner edge (M. A. MacGregor et al. 2017; L. Matrà et al. 2020), while the inner emission observed by MIRI suggests an overabundance of small grains in the inner region that cannot be explained by the same size distribution as in the outer belt seen in ALMA observations. The inner dust has instead been modelled by dust dragged inwards from the outer belt by Poynting-Robertson drag in Fomalhaut (M. Sommer et al. 2025) and Vega (K. Y. L. Su et al. 2024), which very closely reproduces the observations.

γ Oph differs from Fomalhaut and Vega in that the mm-wavelength belt is broad with a shallow inner edge, and that the ALMA and MIRI radial profiles are in fact consistent with a single grain size distribution, without the need to invoke PR drag. A steady-state collisional model consistent between the $15\,\mu\text{m}$, $25\,\mu\text{m}$ and $0.87\,\text{mm}$ is notable as a single power-law grain size model has not been found for other spatially resolved, radially broad disks such as HR 8799 (K. Y. L. Su et al. 2009) and β Pic (N. P. Ballering et al. 2016). γ Oph could therefore be an archetype for a radially broad steady-state collisional cascade.

While the radial profiles suggest that the smaller (micron-sized) grains are no more abundant in the inner disk (within 50 au) than expected from a steady-state collisional cascade from larger (mm-sized) grains (Figs. 7 and 8), uncertainties in this region are large. Noting that Vega and Fomalhaut are close (the 3rd and 4th nearest A stars, both at 7.7 pc), whereas γ Oph is significantly further (the 59th closest A star at 29.7 pc), it is possible that proximity may have more clearly revealed any inner disk formed from PR drag in Vega and Fomalhaut but not in γ Oph.

It is possible that some level of PR-drag dust component is hiding as unresolved dust emission. In γ Oph at $25.5\,\mu\text{m}$, the fitted central point source flux of between 220 and 240 mJy (depending on choice of model) is slightly greater than the stellar component flux of 205 mJy inferred from the SED, suggesting that any unresolved dust is less than approximately 30 mJy. This

level of dust is comparable to the flux density of the inner warm dust component in Fomalhaut and Vega when adjusted for their 4 times closer distance.

Alternatively, the balance between the PR drag timescale and the collisional timescale in γ Oph could have caused PR drag to exert a less prominent effect on the dust distribution. The PR drag timescale in γ Oph, Fomalhaut and Vega are expected to be similar given their comparable stellar masses and luminosities, however the collisional timescale is likely significantly shorter in γ Oph. Given comparable stellar luminosities, a direct comparison of the surface brightness of the the main/outer-belt at ~ 150 au in all three disks shows γ Oph to be over an order of magnitude brighter when adjusted for distance, and thus likely of a significantly higher optical depth. This is supported by optical depth modelling, which infers a six times lower optical depth in the broad outer belt of Vega (K. Y. L. Su et al. 2024) compared to the broad belt of γ Oph. The outer belt of Fomalhaut is narrow, so dust grains are expected to spend more time in the broad inner dust component immediately interior to the main belt, which has a similar optical depth to Vega at 100 au (M. Sommer et al. 2025). As a result, the effective collisional timescale in γ Oph is half an order of magnitude shorter than in Vega and Fomalhaut, which we hypothesise without further modelling could be sufficient to weaken the degree of inward dust transport observed by MIRI (M. C. Wyatt 2005a).

6. CONCLUSIONS

We imaged the debris disk of γ Oph with JWST/MIRI at 15 and 25.5 μm , finding a smooth and radially broad disk with inner emission extending to the star and outer emission detected out to approximately 250 au at 25.5 μm and 150 au at 15 μm . The radial structure of the disk inferred from the MIRI observations, available ALMA imaging (S. Marino et al. 2026) and the SED of the system are consistent with a steady-state collisional cascade characterised by a single power-law grain size distribution throughout the disk, with a minimum grain size within $\sim 10\%$ (just below) the radiation pressure blowout size. This broad consistency suggests that the resolved disk is likely populated by a radially broad planetesimal belt with the observed dust population predominantly formed in situ, rather than displaced by radiative forces.

The disk appears to be azimuthally asymmetric, which can be modelled by a stellocentric offset corresponding to a mild eccentricity of ~ 0.02 . It is plausible for an eccentric giant planet, or a stellar-mass companion within 10 au, to induce this disk eccentricity within the 300 Myr

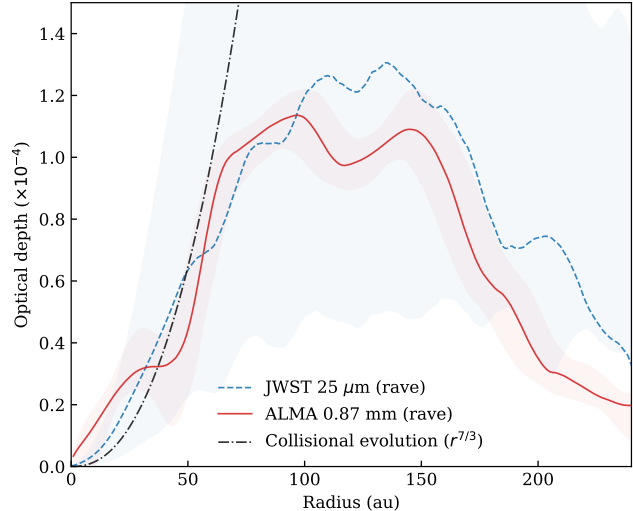


Figure 8. The geometric optical depth profile of the debris disk of γ Oph inferred from surface brightness profiles shown in Fig. 7. These profiles assume a steady-state collisional cascade with a size distribution power-law index of -3.5 between 15 μm and 1 m and a grain composition as described in Section 4.2. The dash-dotted black line corresponds to an inner edge optical depth profile proportional to $r^{7/3}$, as expected of a collisionally evolved broad disk (G. M. Kennedy & M. C. Wyatt 2010).

age of the system without clearing an observable radial gap.

Overall, the observations seem to indicate a broad collisional disk rather than one seen to be broad due to PR drag or radiation pressure, making γ Oph a thus far rare example of a smooth and broad debris disk without significant evidence for radiative transport of dust grains in the mid-infrared. Such a result contrasts with other A stars including Vega (K. Y. L. Su et al. 2024) and Fomalhaut (A. Gáspár et al. 2023), for which MIRI imaging revealed an inner disk component caused by PR drag (M. Sommer et al. 2025). The dense and radially broad nature of the disk in γ Oph could contribute to shorter collisional timescales and thus less prominent effects from PR drag. These results encourage further observational exploration of the diversity of mid-infrared debris disk structures and the dynamical processes to which they are sensitive.

ACKNOWLEDGMENTS

This work is based on observations made with the NASA/ESA/CSA *James Webb Space Telescope*. The data were obtained from the Mikulski Archive for Space Telescopes at the Space Telescope Science Institute, which is operated by the Association of Universities for Research in Astronomy, Inc., under NASA con-

tract NAS 5-03127 for JWST. These observations are associated with program #5709. Support for program #5709 was provided by NASA through a grant from the Space Telescope Science Institute. This research used the Canadian Advanced Network For Astronomy Research (CANFAR) operated in partnership by the Canadian Astronomy Data Centre and The Digital Research Alliance of Canada with support from the National Research Council of Canada the Canadian Space Agency, CANARIE and the Canadian Foundation for Innovation. YH is funded by a Caltech Barr Fellowship. This work was supported by the Science and Technology Facilities Council grant UKRI 1158. AAS is supported by the Heising-Simons Foundation through a 51 Pegasi b Fellowship. JBL acknowledges the Smithsonian Institute for funding via a Submillimeter Array (SMA) Fellowship. CdB acknowledges support from the Spanish Ministerio de Ciencia, Innovación y Universidades (MICIU) and the European Regional Development Fund (ERDF) under reference PID2023-153342NB-I00/10.13039/501100011033, from the Beatriz Galindo Senior Fellowship BG22/00166 funded by the MICIU, and the support from the Universidad de La Laguna (ULL) and the Consejería de Economía, Conocimiento y Empleo of the Gobierno de Canarias. JPM acknowledges research support by the National

Science and Technology Council of Taiwan under grant NSTC 112-2112-M-001-032-MY3. SM acknowledges funding by the Royal Society through a Royal Society University Research Fellowship (URF-R1-221669) and the European Union through the FEED ERC project (grant number 101162711). Views and opinions expressed are however those of the author(s) only and do not necessarily reflect those of the European Union or the European Research Council Executive Agency. Neither the European Union nor the granting authority can be held responsible for them. AMH gratefully acknowledges support from the National Science Foundation under Grant No. AST-2307920.

AUTHOR CONTRIBUTIONS

YH planned the observations and wrote the manuscript. All authors contributed to proposal preparation and manuscript editing.

Facilities: JWST(MIRI), ALMA

Software: NumPy (C. R. Harris et al. 2020), SciPy (P. Virtanen et al. 2020), Matplotlib (J. D. Hunter 2007), Astropy (Astropy Collaboration et al. 2022), JWST Science Calibration Pipeline (H. Bushouse et al. 2025)

APPENDIX

A. AZIMUTHALLY AVEVRAGED PROFILE

The azimuthally averaged radial profiles measured from the images are shown in Fig. 9.

REFERENCES

Argyriou, I., Lage, C., Rieke, G. H., et al. 2023, A&A, 680, A96, doi: [10.1051/0004-6361/202346490](https://doi.org/10.1051/0004-6361/202346490)

Astropy Collaboration, Price-Whelan, A. M., Lim, P. L., et al. 2022, ApJ, 935, 167, doi: [10.3847/1538-4357/ac7c74](https://doi.org/10.3847/1538-4357/ac7c74)

Ballering, N. P., Su, K. Y. L., Rieke, G. H., & Gáspár, A. 2016, ApJ, 823, 108, doi: [10.3847/0004-637X/823/2/108](https://doi.org/10.3847/0004-637X/823/2/108)

Bohren, C. F., & Huffman, D. R. 1983, Absorption and scattering of light by small particles (Wiley)

Burns, J. A., Lamy, P. L., & Soter, S. 1979, Icarus, 40, 1, doi: [10.1016/0019-1035\(79\)90050-2](https://doi.org/10.1016/0019-1035(79)90050-2)

Bushouse, H., Eisenhamer, J., Dencheva, N., et al. 2025, JWST Calibration Pipeline, 1.18.0 Zenodo, doi: [10.5281/zenodo.6984365](https://doi.org/10.5281/zenodo.6984365)

Chelli, A., Duvert, G., Bourgès, L., et al. 2016, A&A, 589, A112, doi: [10.1051/0004-6361/201527484](https://doi.org/10.1051/0004-6361/201527484)

Chen, C. H., Mittal, T., Kuchner, M., et al. 2014, ApJS, 211, 25, doi: [10.1088/0067-0049/211/2/25](https://doi.org/10.1088/0067-0049/211/2/25)

Cutri, R. M., Skrutskie, M. F., van Dyk, S., et al. 2003, 2MASS All Sky Catalog of point sources.,

Daley, C., Hughes, A. M., Carter, E. S., et al. 2019, ApJ, 875, 87, doi: [10.3847/1538-4357/ab1074](https://doi.org/10.3847/1538-4357/ab1074)

David, T. J., & Hillenbrand, L. A. 2015, ApJ, 804, 146, doi: [10.1088/0004-637X/804/2/146](https://doi.org/10.1088/0004-637X/804/2/146)

Dohnanyi, J. S. 1969, J. Geophys. Res., 74, 2531, doi: [10.1029/JB074i010p02531](https://doi.org/10.1029/JB074i010p02531)

Eiroa, C., Marshall, J. P., Mora, A., et al. 2013, A&A, 555, A11, doi: [10.1051/0004-6361/201321050](https://doi.org/10.1051/0004-6361/201321050)

ESA, ed. 1997, ESA Special Publication, Vol. 1200, The HIPPARCOS and TYCHO catalogues. Astrometric and photometric star catalogues derived from the ESA HIPPARCOS Space Astrometry Mission

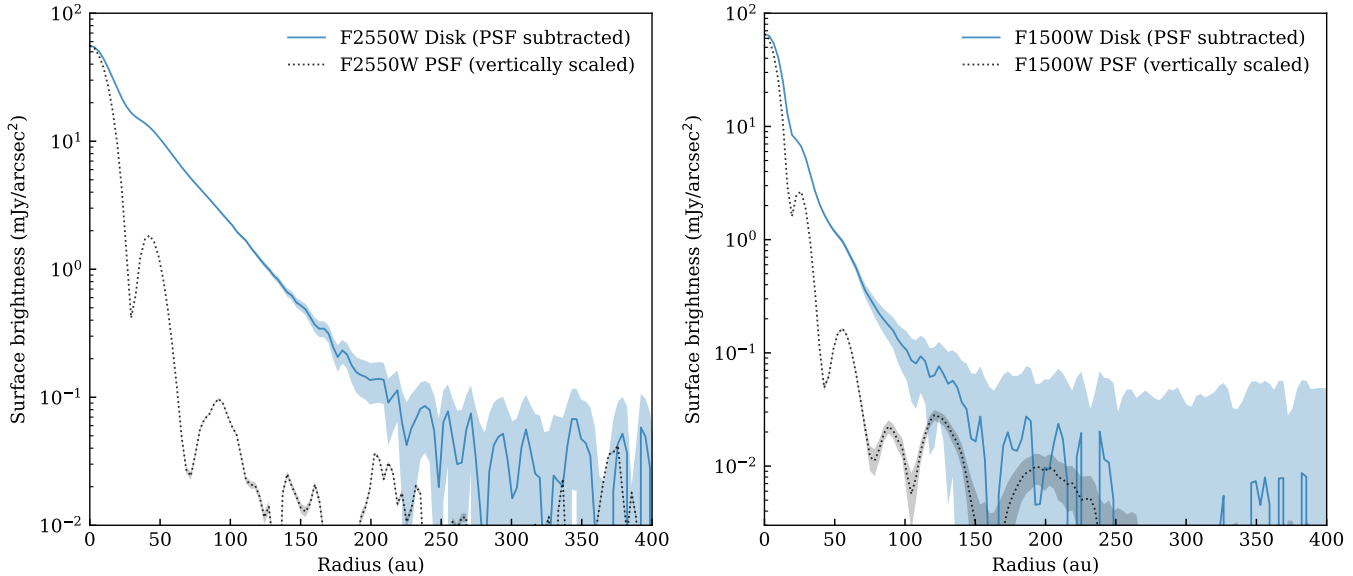


Figure 9. The azimuthally averaged F2550W (left) and F1500W (right) radial profiles measured from the PSF-subtracted (assuming SED flux) image, which are displayed in solid blue lines. The black dotted lines correspond to the PSF observations scaled to match the radial profile of the disk at its centre.

Farhat, M. A., Sefilian, A. A., & Touma, J. R. 2023, MNRAS, 521, 2067, doi: [10.1093/mnras/stad316](https://doi.org/10.1093/mnras/stad316)

Foreman-Mackey, D., Hogg, D. W., Lang, D., & Goodman, J. 2013, PASP, 125, 306, doi: [10.1086/670067](https://doi.org/10.1086/670067)

Friebe, M. F., Pearce, T. D., & Löhne, T. 2022, MNRAS, 512, 4441, doi: [10.1093/mnras/stac664](https://doi.org/10.1093/mnras/stac664)

Gaia Collaboration, Brown, A. G. A., Vallenari, A., et al. 2018, A&A, 616, A1, doi: [10.1051/0004-6361/201833051](https://doi.org/10.1051/0004-6361/201833051)

Gáspár, A., Rieke, G. H., & Ballering, N. 2016, ApJ, 826, 171, doi: [10.3847/0004-637X/826/2/171](https://doi.org/10.3847/0004-637X/826/2/171)

Gáspár, A., Su, K. Y. L., Rieke, G. H., et al. 2008, ApJ, 672, 974, doi: [10.1086/523299](https://doi.org/10.1086/523299)

Gáspár, A., Wolff, S. G., Rieke, G. H., et al. 2023, Nature Astronomy, 7, 790, doi: [10.1038/s41550-023-01962-6](https://doi.org/10.1038/s41550-023-01962-6)

Geiler, F., Krivov, A. V., Booth, M., & Löhne, T. 2019, MNRAS, 483, 332, doi: [10.1093/mnras/sty3160](https://doi.org/10.1093/mnras/sty3160)

Han, Y., Mansell, E., Jennings, J., et al. 2026, A&A, 705, A196, doi: [10.1051/0004-6361/202556450](https://doi.org/10.1051/0004-6361/202556450)

Han, Y., Wyatt, M. C., & Marino, S. 2025, MNRAS, doi: [10.1093/mnras/staf282](https://doi.org/10.1093/mnras/staf282)

Han, Y., Wyatt, M. C., & Matrà, L. 2022, MNRAS, 511, 4921, doi: [10.1093/mnras/stac373](https://doi.org/10.1093/mnras/stac373)

Han, Y., Wyatt, M., Carpenter, J., et al. 2024, What causes warm dust interior to planetesimal belts?., JWST Proposal. Cycle 3, ID. #5709

Harris, C. R., Millman, K. J., van der Walt, S. J., et al. 2020, Nature, 585, 357–362, doi: [10.1038/s41586-020-2649-2](https://doi.org/10.1038/s41586-020-2649-2)

Hines, D. C., Schneider, G., Hollenbach, D., et al. 2007, ApJL, 671, L165, doi: [10.1086/525016](https://doi.org/10.1086/525016)

Høg, E., Fabricius, C., Makarov, V. V., et al. 2000, A&A, 355, L27

Holland, W. S., Matthews, B. C., Kennedy, G. M., et al. 2017, MNRAS, 470, 3606, doi: [10.1093/mnras/stx1378](https://doi.org/10.1093/mnras/stx1378)

Hughes, A. M., Duchêne, G., & Matthews, B. C. 2018, ARAA, 56, 541, doi: [10.1146/annurev-astro-081817-052035](https://doi.org/10.1146/annurev-astro-081817-052035)

Hunter, J. D. 2007, Computing In Science & Engineering, 9, 90

Husser, T. O., Wende-von Berg, S., Dreizler, S., et al. 2013, A&A, 553, A6, doi: [10.1051/0004-6361/201219058](https://doi.org/10.1051/0004-6361/201219058)

Imaz Blanco, A., Marino, S., Matrà, L., et al. 2023, MNRAS, 522, 6150, doi: [10.1093/mnras/stad1221](https://doi.org/10.1093/mnras/stad1221)

IRSA, & SSC. 2020, Spitzer Enhanced Imaging Products., NASA IPAC DataSet, IRSA433 doi: [10.26131/IRSA433](https://doi.org/10.26131/IRSA433)

Ishihara, D., Onaka, T., Kataza, H., et al. 2010, A&A, 514, A1, doi: [10.1051/0004-6361/200913811](https://doi.org/10.1051/0004-6361/200913811)

Jankovic, M. R., Pawellek, N., Zander, J., et al. 2026, A&A, 705, A204, doi: [10.1051/0004-6361/202556637](https://doi.org/10.1051/0004-6361/202556637)

Jankovic, M. R., Wyatt, M. C., & Löhne, T. 2024, A&A, 691, A302, doi: [10.1051/0004-6361/202451080](https://doi.org/10.1051/0004-6361/202451080)

Jennings, J., Booth, R. A., Tazzari, M., Rosotti, G. P., & Clarke, C. J. 2020, MNRAS, 495, 3209, doi: [10.1093/mnras/staa1365](https://doi.org/10.1093/mnras/staa1365)

Kennedy, G. M., & Wyatt, M. C. 2010, MNRAS, 405, 1253, doi: [10.1111/j.1365-2966.2010.16528.x](https://doi.org/10.1111/j.1365-2966.2010.16528.x)

Kervella, P., Arenou, F., & Thévenin, F. 2022, *A&A*, 657, A7, doi: [10.1051/0004-6361/202142146](https://doi.org/10.1051/0004-6361/202142146)

Krivov, A. V. 2010, *Research in Astronomy and Astrophysics*, 10, 383, doi: [10.1088/1674-4527/10/5/001](https://doi.org/10.1088/1674-4527/10/5/001)

Krivov, A. V., & Wyatt, M. C. 2021, *MNRAS*, 500, 718, doi: [10.1093/mnras/staa2385](https://doi.org/10.1093/mnras/staa2385)

Lee, E. J., & Chiang, E. 2016, *ApJ*, 827, 125, doi: [10.3847/0004-637X/827/2/125](https://doi.org/10.3847/0004-637X/827/2/125)

Li, A., & Greenberg, J. M. 1997, *A&A*, 323, 566

Lovell, J. B., Hales, A. S., Kennedy, G. M., et al. 2026, *A&A*, 705, A200, doi: [10.1051/0004-6361/202556568](https://doi.org/10.1051/0004-6361/202556568)

Lovell, J. B., & Lynch, E. M. 2023, *MNRAS*, 525, L36, doi: [10.1093/mnrasl/slad083](https://doi.org/10.1093/mnrasl/slad083)

Lovell, J. B., Marino, S., Wyatt, M. C., et al. 2021, *MNRAS*, 506, 1978, doi: [10.1093/mnras/stab1678](https://doi.org/10.1093/mnras/stab1678)

Lynch, E. M., & Lovell, J. B. 2022, *MNRAS*, 510, 2538, doi: [10.1093/mnras/stab3566](https://doi.org/10.1093/mnras/stab3566)

MacGregor, M. A., Matrà, L., Kalas, P., et al. 2017, *ApJ*, 842, 8, doi: [10.3847/1538-4357/aa71ae](https://doi.org/10.3847/1538-4357/aa71ae)

MacGregor, M. A., Weinberger, A. J., Nesvold, E. R., et al. 2019, *ApJL*, 877, L32, doi: [10.3847/2041-8213/ab21c2](https://doi.org/10.3847/2041-8213/ab21c2)

Malhotra, R. 1993, *Nature*, 365, 819, doi: [10.1038/365819a0](https://doi.org/10.1038/365819a0)

Mamajek, E. E. 2012, *ApJL*, 754, L20, doi: [10.1088/2041-8205/754/2/L20](https://doi.org/10.1088/2041-8205/754/2/L20)

Marino, S. 2021, *MNRAS*, 503, 5100, doi: [10.1093/mnras/stab771](https://doi.org/10.1093/mnras/stab771)

Marino, S., Matrà, L., Hughes, A. M., et al. 2026, *A&A*, 705, A195, doi: [10.1051/0004-6361/202556489](https://doi.org/10.1051/0004-6361/202556489)

Marino, S., Yelverton, B., Booth, M., et al. 2019, *MNRAS*, 484, 1257, doi: [10.1093/mnras/stz049](https://doi.org/10.1093/mnras/stz049)

Marino, S., Carpenter, J., Wyatt, M. C., et al. 2018, *MNRAS*, 479, 5423, doi: [10.1093/mnras/sty1790](https://doi.org/10.1093/mnras/sty1790)

Marino, S., Zurlo, A., Faramaz, V., et al. 2020, *MNRAS*, 498, 1319, doi: [10.1093/mnras/staa2386](https://doi.org/10.1093/mnras/staa2386)

Marshall, J. P., Muñoz-Gutiérrez, M. A., Sefilian, A. A., & Peimbert, A. 2025a, *MNRAS*, doi: [10.1093/mnras/staf1990](https://doi.org/10.1093/mnras/staf1990)

Marshall, J. P., Wang, L., Kennedy, G. M., Zeegers, S. T., & Scicluna, P. 2021, *MNRAS*, 501, 6168, doi: [10.1093/mnras/staa3917](https://doi.org/10.1093/mnras/staa3917)

Marshall, J. P., Milli, J., Choquet, E., et al. 2023, *MNRAS*, 521, 5940, doi: [10.1093/mnras/stad913](https://doi.org/10.1093/mnras/stad913)

Marshall, J. P., Hengst, S., Young, R., et al. 2025b, *MNRAS*, doi: [10.1093/mnras/staf2221](https://doi.org/10.1093/mnras/staf2221)

Matrà, L., Wyatt, M. C., Wilner, D. J., et al. 2019, *AJ*, 157, 135, doi: [10.3847/1538-3881/ab06c0](https://doi.org/10.3847/1538-3881/ab06c0)

Matrà, L., Dent, W. R. F., Wilner, D. J., et al. 2020, *ApJ*, 898, 146, doi: [10.3847/1538-4357/aba0a4](https://doi.org/10.3847/1538-4357/aba0a4)

Matrà, L., Marino, S., Wilner, D. J., et al. 2025, *A&A*, 693, A151, doi: [10.1051/0004-6361/202451397](https://doi.org/10.1051/0004-6361/202451397)

Mermilliod, J. C. 2006, *VizieR Online Data Catalog: Homogeneous Means in the UBV System (Mermilliod 1991)*, *VizieR On-line Data Catalog: II/168*. Originally published in: Institut d'Astronomie, Universite de Lausanne (1991)

Milli, J., Olofsson, J., Bonduelle, M., et al. 2026, *A&A*, 705, A199, doi: [10.1051/0004-6361/202556523](https://doi.org/10.1051/0004-6361/202556523)

Moór, A., Kóspál, Á., Ábrahám, P., et al. 2015, *MNRAS*, 447, 577, doi: [10.1093/mnras/stu2442](https://doi.org/10.1093/mnras/stu2442)

Morbidelli, A., Emel'yanenko, V. V., & Levison, H. F. 2004, *MNRAS*, 355, 935, doi: [10.1111/j.1365-2966.2004.08372.x](https://doi.org/10.1111/j.1365-2966.2004.08372.x)

Morrison, S., & Malhotra, R. 2015, *ApJ*, 799, 41, doi: [10.1088/0004-637X/799/1/41](https://doi.org/10.1088/0004-637X/799/1/41)

Murray, C. D., & Dermott, S. F. 1999, *Solar System Dynamics*, doi: [10.1017/CBO9781139174817](https://doi.org/10.1017/CBO9781139174817)

Mustill, A. J., & Wyatt, M. C. 2012, *MNRAS*, 419, 3074, doi: [10.1111/j.1365-2966.2011.19948.x](https://doi.org/10.1111/j.1365-2966.2011.19948.x)

Nederlander, A., Hughes, A. M., Fehr, A. J., et al. 2021, *ApJ*, 917, 5, doi: [10.3847/1538-4357/abdd32](https://doi.org/10.3847/1538-4357/abdd32)

Nilsson, R., Liseau, R., Brandeker, A., et al. 2010, *A&A*, 518, A40, doi: [10.1051/0004-6361/201014444](https://doi.org/10.1051/0004-6361/201014444)

Olofsson, J., Thébault, P., Kennedy, G. M., & Bayo, A. 2022, *A&A*, 664, A122, doi: [10.1051/0004-6361/202243794](https://doi.org/10.1051/0004-6361/202243794)

Olofsson et al., J. submitted, *A&A*

Pan, M., & Schlichting, H. E. 2012, *ApJ*, 747, 113, doi: [10.1088/0004-637X/747/2/113](https://doi.org/10.1088/0004-637X/747/2/113)

Pawellek, N., & Krivov, A. V. 2015, *MNRAS*, 454, 3207, doi: [10.1093/mnras/stv2142](https://doi.org/10.1093/mnras/stv2142)

Pawellek, N., Krivov, A. V., Marshall, J. P., et al. 2014, *ApJ*, 792, 65, doi: [10.1088/0004-637X/792/1/65](https://doi.org/10.1088/0004-637X/792/1/65)

Pearce, T. D., & Wyatt, M. C. 2014, *MNRAS*, 443, 2541, doi: [10.1093/mnras/stu1302](https://doi.org/10.1093/mnras/stu1302)

Pearce, T. D., Krivov, A. V., Sefilian, A. A., et al. 2024, *MNRAS*, 527, 3876, doi: [10.1093/mnras/stad3462](https://doi.org/10.1093/mnras/stad3462)

Pilbratt, G. L., Riedinger, J. R., Passvogel, T., et al. 2010, *A&A*, 518, L1, doi: [10.1051/0004-6361/201014759](https://doi.org/10.1051/0004-6361/201014759)

Plavchan, P., Jura, M., & Lipsky, S. J. 2005, *ApJ*, 631, 1161, doi: [10.1086/432568](https://doi.org/10.1086/432568)

Schneider, G., Grady, C. A., Hines, D. C., et al. 2014, *AJ*, 148, 59, doi: [10.1088/0004-6256/148/4/59](https://doi.org/10.1088/0004-6256/148/4/59)

Sefilian, A. A. 2024, *ApJ*, 966, 140, doi: [10.3847/1538-4357/ad32d1](https://doi.org/10.3847/1538-4357/ad32d1)

Sefilian, A. A., Kratter, K. M., Wyatt, M. C., et al. 2025, *MNRAS*, 543, 3123, doi: [10.1093/mnras/staf1555](https://doi.org/10.1093/mnras/staf1555)

Sefilian, A. A., Rafikov, R. R., & Wyatt, M. C. 2021, *ApJ*, 910, 13, doi: [10.3847/1538-4357/abda46](https://doi.org/10.3847/1538-4357/abda46)

Sefilian, A. A., Rafikov, R. R., & Wyatt, M. C. 2023, *ApJ*, 954, 100, doi: [10.3847/1538-4357/ace68e](https://doi.org/10.3847/1538-4357/ace68e)

Shannon, A., Bonsor, A., Kral, Q., & Matthews, E. 2016, MNRAS, 462, L116, doi: [10.1093/mnrasl/slw143](https://doi.org/10.1093/mnrasl/slw143)

Sommer, M., Wyatt, M., & Han, Y. 2025, MNRAS, 539, 439, doi: [10.1093/mnras/staf494](https://doi.org/10.1093/mnras/staf494)

Stapelfeldt, K. R., Holmes, E. K., Chen, C., et al. 2004, ApJS, 154, 458, doi: [10.1086/423135](https://doi.org/10.1086/423135)

Strubbe, L. E., & Chiang, E. I. 2006, ApJ, 648, 652, doi: [10.1086/505736](https://doi.org/10.1086/505736)

Su, K. Y. L., Rieke, G. H., Stapelfeldt, K. R., et al. 2008, ApJL, 679, L125, doi: [10.1086/589508](https://doi.org/10.1086/589508)

Su, K. Y. L., Rieke, G. H., Misselt, K. A., et al. 2005, ApJ, 628, 487, doi: [10.1086/430819](https://doi.org/10.1086/430819)

Su, K. Y. L., Rieke, G. H., Stansberry, J. A., et al. 2006, ApJ, 653, 675, doi: [10.1086/508649](https://doi.org/10.1086/508649)

Su, K. Y. L., Rieke, G. H., Stapelfeldt, K. R., et al. 2009, ApJ, 705, 314, doi: [10.1088/0004-637X/705/1/314](https://doi.org/10.1088/0004-637X/705/1/314)

Su, K. Y. L., Gáspár, A., Rieke, G. H., et al. 2024, ApJ, 977, 277, doi: [10.3847/1538-4357/ad8cde](https://doi.org/10.3847/1538-4357/ad8cde)

Terrill, J., Marino, S., Booth, R. A., et al. 2023, MNRAS, 524, 1229, doi: [10.1093/mnras/stad1847](https://doi.org/10.1093/mnras/stad1847)

Thébault, P., & Augereau, J.-C. 2007, A&A, 472, 169, doi: [10.1051/0004-6361:20077709](https://doi.org/10.1051/0004-6361:20077709)

Thebault, P., & Kral, Q. 2019, A&A, 626, A24, doi: [10.1051/0004-6361/201935341](https://doi.org/10.1051/0004-6361/201935341)

Vican, L. 2012, AJ, 143, 135, doi: [10.1088/0004-6256/143/6/135](https://doi.org/10.1088/0004-6256/143/6/135)

Virtanen, P., Gommers, R., Oliphant, T. E., et al. 2020, Nature Methods, 17, 261, doi: [10.1038/s41592-019-0686-2](https://doi.org/10.1038/s41592-019-0686-2)

Vizgan, D., Hughes, A. M., Carter, E. S., et al. 2022, ApJ, 935, 131, doi: [10.3847/1538-4357/ac80b8](https://doi.org/10.3847/1538-4357/ac80b8)

Williams, J. P., & Cieza, L. A. 2011, ARA&A, 49, 67, doi: [10.1146/annurev-astro-081710-102548](https://doi.org/10.1146/annurev-astro-081710-102548)

Wisdom, J. 1980, AJ, 85, 1122, doi: [10.1086/112778](https://doi.org/10.1086/112778)

Wolff, S. G., Gáspár, A., Rieke, G., et al. 2025, AJ, 170, 244, doi: [10.3847/1538-3881/adfcfd6](https://doi.org/10.3847/1538-3881/adfcfd6)

Wright, E. L., Eisenhardt, P. R. M., Mainzer, A. K., et al. 2010, AJ, 140, 1868, doi: [10.1088/0004-6256/140/6/1868](https://doi.org/10.1088/0004-6256/140/6/1868)

Wright, G. S., Rieke, G. H., Glasse, A., et al. 2023, PASP, 135, 048003, doi: [10.1088/1538-3873/acbe66](https://doi.org/10.1088/1538-3873/acbe66)

Wyatt, M. C. 2005a, A&A, 433, 1007, doi: [10.1051/0004-6361:20042073](https://doi.org/10.1051/0004-6361:20042073)

Wyatt, M. C. 2005b, A&A, 440, 937, doi: [10.1051/0004-6361:20053391](https://doi.org/10.1051/0004-6361:20053391)

Wyatt, M. C. 2008, ARA&A, 46, 339, doi: [10.1146/annurev.astro.45.051806.110525](https://doi.org/10.1146/annurev.astro.45.051806.110525)

Wyatt, M. C., Dermott, S. F., Telesco, C. M., et al. 1999, ApJ, 527, 918, doi: [10.1086/308093](https://doi.org/10.1086/308093)

Wyatt, M. C., Smith, R., Su, K. Y. L., et al. 2007, ApJ, 663, 365, doi: [10.1086/518404](https://doi.org/10.1086/518404)

Yelverton, B., & Kennedy, G. M. 2018, MNRAS, 479, 2673, doi: [10.1093/mnras/sty1678](https://doi.org/10.1093/mnras/sty1678)

Yoon, J., Peterson, D. M., Kurucz, R. L., & Zagarello, R. J. 2010, ApJ, 708, 71, doi: [10.1088/0004-637X/708/1/71](https://doi.org/10.1088/0004-637X/708/1/71)

Zawadzki, B., Fehr, A., Hughes, A. M., et al. 2026, A&A, 705, A197, doi: [10.1051/0004-6361/202556505](https://doi.org/10.1051/0004-6361/202556505)